Low temperature Terahertz Spectroscopy of $LaFeO_3$, $PrFeO_3$, $ErFeO_3$, and $LuFeO_3$: magnon resonances and ground multiplet transitions

Néstor E. Massa,*[,1] Leire del Campo,[2] Vinh Ta Phuoc,[3] Paula Kayser,[4,‡] and José Antonio Alonso[5]

[1] Centro CEQUINOR, Consejo Nacional de Investigaciones Científicas y Técnicas, Universidad Nacional de La Plata, Bv. 120 1465, B1904 La Plata, Argentina.

[2]Centre National de la Recherche Scientifique, CEMHTI UPR3079, Université Orléans, F-45071 Orléans, France.

[3]Groupement de Recherche Matériaux Microélectronique Acoustique Nanotechnologies-Université François Rabelais Tours, Faculté des Sciences & Techniques, F- 37200 Tours, France.

[4]Centre for Science at Extreme Conditions and School of Chemistry, University of Edinburgh, Kings Buildings, Mayfield Road, EH9 3FD Edinburgh, United Kingdom.

[5]Instituto de Ciencia de Materiales de Madrid, CSIC, Cantoblanco, E-28049 Madrid, Spain.

‡Present address: Departamento de Química Inorgánica, Facultad de Ciencias Químicas, Universidad Complutense de Madrid, 28040 Madrid, Spain.

Corresponding author:
*Néstor E. Massa, e-mail: neemmassa@gmail.com

Physics Subject Headings (PhySH)

Research Areas

Spin wave resonances. Magnons. Magnetic anisotropy. Canted ferromagnetism., Antiferromagnetism. Ferroelectricity. Optical phonons.

Physical Systems

Ferrites. Multiferroics. Strongly correlated systems. Perovskites.

Techniques

Optically detected magnetic resonances. Crystal field theory. Terahertz spectroscopy. Fourier transform infrared spectroscopy

DISCIPLINE

Condensed Matter, Materials & Applied Physics

Abstract

We report on zone center THz excitations of non--Jahn Teller $LaFeO_3$, $PrFeO_3$, $ErFeO_3$, and $LuFeO_3$ distorted perovskites under external magnetic fields up 7 T. Our measurements on low temperature-low energy absorptions of $LaFeO_3$ show antiferromagnetic and ferromagnetic magnons at ω_{AFM}~31.4 and ω_{FM} ~26.7 cm^{-1} in the Γ_4 (G_x, A_y, F_z) representation with degeneracy near linearly lifted by the field. $LuFeO_3$ is characterized by zero field magnetic resonances at ω_{AFM} ~26.3 cm^{-1} and ω_{FM} ~22.4 cm^{-1} in addition to Fe^{3+} Zeeman -split crystal field (CF) $6A_1$ ground transitions at ~10.4 cm^{-1} triggered by subtle structural deviations induced by the Lu $4f^{14}$ smaller ionic radius at the A site. This local quasi-non-centrosymmetric departure is also found in $ErFeO_3$ (Kramers $4f^{11}$ Er^{3+} ($^4I_{15/2}$); Γ_2 (F_x, C_y, G_z) <T_{SR} ~93 K), but with the ~4 cm^{-1} Fe^{3+} Zeeman branching strongly biased toward higher energies due to 3d-4f exchange. Magnons at ω_{AFM} ~31.5 cm^{-1} and ω_{FM} ~21.5 cm^{-1} in $ErFeO_3$ do not undergo field induced band splits but a 13-fold increase in the antiferro (ω_{AMF}) /ferro(ω_{AFM}) intensity ratio. There is a remarkable field-dependent CF matching population balance between Fe^{3+} higher and Er^{3+} lower Zeeman branches. The Er^{3+} ($^4I_{15/2}$) multiplet, at the 49.5 cm^{-1}, 110.5 cm^{-1}, and 167.3 cm^{-1}, coincides with external lattice mode frequencies suggesting strong lattice driven spin-phonon interactions. Far infrared absorption ratios under mild external fields reveal magnetic dependence only for those zone center phonons involving moving magnetic ions.

Antiferro- and ferro- resonances in $PrFeO_3$ turn much broader as non-Kramers Pr^3 introduces ligand changes at the A site leading into near degeneracy the antiferromagnetic mode and the lowest Pr^{3+} CF transition. They merge into a single broad mostly unresolved feature at 7 T.

We conclude that low energy excitations in $RFeO_3$ (R=rare earth) strongly depend on the lanthanide ionic size thus indivisibly tied to the mechanism associated to the origin of canted ferromagnetism. In addition, minute lattice displacements also underlie considering non-centrosymmetric the most distorted $RFeO_3$ (R=rare earth). In these perovskites the changes triggered in the lattice by the smaller rare earth and the nonlinear intrinsic oxygen ion polarizability, known to drive lattice instabilities, provide grounds for interplay of ionic and electronic interactions yielding ferroelectric spontaneous polarization.

.

INTRODUCTION

The search of multifunctional materials with magnetic and electronic polarizations as in ferromagnetic ferroelectric multiferroics [1] contributed in the last decades to advances in material development aiming to devices that would potentially perform more than one task [2]. $RFeO_3$ (R=rare earth) is one family of these compounds sustaining a distorted cubic perovskite lattice. Increasing the degree of octahedral tilting across the series was early recognized to accommodate structural distortions and interplays in a unique magnetic and electronic environment created by the Fe^{3+} and R^{3+} ions [3-6]. These cooperative exchanges may then be incorporated to developments that would change our way of life as in the proposed magnetizable concrete for road electrification aimed to vehicle "on the road" charging [7].

The rich magnetic phase diagram of $RFeO_3$ originates in the Fe^{3+} and R^{3+} independent magnetic sublattices containing Fe^{3+} canted spins tangled to iron's magnetic order and 4f lanthanide exchanges promoting magnetoelectric couplings. The consequences of this appear as changes in phonon transverse optical-longitudinal optical (TO-LO) macroscopic field magnetic and electric dependences [8, 9], Heisenberg magnons [10], crystal field (CF) levels, and in Fe^{3+} canted magnons within the spectral region from far infrared to the THz.

$RFeO_3$ ferrites, with four molecule per unit cell (Z=4), belong to the room temperature crystalline space group Pbmn (D_{2h}^{16}) [11] with Fe^{3+} $3d^5$ in a S=5/2 spin moment high state configuration. Below their Nèel temperatures T_N [12], Fe^{3+} is centrally located in a cage made of 6 antiparallel nearest neighbors facing each other in an isotropic antiferromagnetic coupling. This represents the strongest magnetic interaction in the type G plane arrangement of the Γ_4 (G_x, A_y, F_z) representation meaning a G_x antiferromagnetic ground state along the ***a***-axis, an A_y weak antiferromagnetism along the ***b***-axis, and a F_z weak canted ferromagnetism along the ***c***-axis [13, 14]**.** Next in strength is the Fe^{3+}-R^{3+} exchange followed by the weaker antiferromagnetic R^{3+}- R^{3+} interaction found at low temperatures when paramagnetic rare earth moment turn ordered in an environment of complex exchanges that may include exchange mediated out of ***ac*** plane magnetic components as for in the Γ_1 (A_x, G_y, C_z) representation. (Fig. S1)

The distinctive F_z ferromagnetic component in Γ_4 (G_x, A_y, F_z) along the <u>*c*</u> axis originates in non-collinear spin canting with out of the plane deviations of the order of less than 1◦. Regardless of the prevalent mechanism for the origin of canted ferromagnetism, either from Dzyalonshinkii-Moriya antisymmetric spin exchanges [15,16] or rare earth induced lattice anisotropies [17], existing R^{3+} moments always have a finite exchange within Fe^{3+} crystal field (CF) in the octahedral sublattice [18]. This triggers spontaneous reorientation (SR) of the iron moments when the field is just large enough to pull the net moment parallel to c axis [19], and as consequence, a non-zero *f*-R^{3+}–rare earth magnetic moment and *d*-M^{3+} exchange reorient, on cooling, G antiferromagnetism and canted ferromagnetism from room temperature Γ_4 (G_x, A_y, F_z) to the lower temperature representation Γ_2 (F_x, C_y, G_z) [20, 21]

Low energy spin wave Fe^{3+} magnetic excitations are zone center precession modes associated to canting that appear in the THz as weak absorptions when stimulated by the infrared light ac magnetic field (Fig. S2). They are named in orthorhombic distorted perovskites, antiferromagnetic (ω_{AMF}) and ferromagnetic (ω_{FM}) modes detectable when the oscillating frequency of the light matches the zone center frequency of spin wave cooperative motions [22**]**. Each resonance is coupled to an exchange mode so that their optical activity is not confined to a specified crystallographic direction and thus they should not view as normal modes [23**]**. One mode (ω_{AFM}) depends on anisotropies in the ***<u>ac</u>*** plane along the antiferromagnetic axis, with the spins net sum in this plane, while the other (ω_{FM}) aligns along the ferromagnetic ***<u>c</u>*** axis performing the net spin rocking motion following the motion of the sublattice spins [24, 25, 26**]**.

Keffer and Kittel [27**]** and Nagamiya [28**]** addressed these $k \approx 0$ magnon resonances with a simplifying approach in which room temperature $\Gamma_4(A_y)$ and low temperature $\Gamma_2(C_y)$ spin deviations were neglected. This results in a de facto reduction of the inequivalent number of molecules per unit cell in the magnetic structure from four magnetic sublattices of the d subsystem M_i (i = 1,…, 4) and four rare-earth sublattices m_j (j = 1, …, 4) to two with individual Fe^{3+} magnetic moments Mj (j= 1-4) bound by the equivalencies M_1=M_3 and M_2=M_4 in the so-called two-sublattice approximation. Accordingly, each magnetization from the two magnetic sublattices along narrow optical orbitals is named M_1 and M_2 and has its equation of motion linked by an exchange interaction that describes unequal precessions triggering the two resonant energy modes function of exchange and anisotropy fields in the orthorhombic lattice [29].

These collective spin excitations have been widely studied from the early days by many material research groups working with non-collinear antiferromagnets [23, 24] Among them, White et al [26] and Koshizuka et al [30, 31] reported temperature dependent Raman scattering of $YFeO_3$, $SmFeO_3$, $DyFeO_3$, $HoFeO_3$, and $ErFeO_3$ and Koslov et al pioneered THz techniques measuring $RFeO_3$ (R=Y, Tm, Dy, Gd, Ho, Er, Tb) [32]. Constable et al [33] and Jiang et al [34] studied the temperature-dependent spin waves and neutron scattering and spin reorientation in $NdFeO_3$ respectively; Fu et al [35] measured spin resonances in $SmFeO_3$, and Zhang et al did it in $TmFeO_3$ using terahertz time domain spectroscopy [36] $YFeO_3$ zone center two spin wave modes have been studied up to17 T by Amelin et al [37**]** and Li et al [38**]** proposed a studied on cooperative exchange coupling of a spin ensemble in Y doped $ErFeO_3$. More recently, the spin dynamics of $TmFeO_3$ [39] and $TbFeO_3$ [40] have been addressed by neutron spectroscopies.

The low energy spin precession modes share the THz spectral region with transition metal CF ground transitions linked to local distortions and sublattice tilted angles that in turn also depend on less prone to modify chemical bond rare earths.

Early diffraction measurements on $RFeO_3$ (R= rare earth) ferrites [11, 41, 42**]** showed that the A polyhedral sites have an anomalous decrease in the number of rare earth-oxygen nearest neighbors that, deviating from the higher temperature cubic phase AO_{12} cage, changes from 10 in $LaFeO_3$ to 6 in $LuFeO_3$ (Fig. 1). The reduction of the Fe-O-Fe "θ" bond angle from 157° in $LaFeO_3$ to 142° in $LuFeO_3$ implies subtle changes in orbital and spin ordering [43-47] that is mirrored in the Néel temperature depending linearly on the Fe-O-Fe superexchange angle and thus on the rare earth cation size [48**].**

The proven lattice ductility of distorted perovskites has profound implications for enabling B site crystal field symmetry forbidden Fe^{3+} transitions of the $^6A_1$ multiplet. As we detail in the following sections, Fe^{3+} ground state Zeeman split transitions is a distinctive feature of the $LuFeO_3$ THz spectra that weighs additionally to the sole spin modes picture found in $LaFeO_3$ that, having a lattice closer to cubic, prevents Fe^{3+} CF transitions becoming optically active. Although both compounds share the P_{bnm} (D^{2h}_{16}) space group, the Fe^{3+} site point group in $LuFeO_3$ is altered by the ligand distortions due to Lu^{3+} smaller ionic radius in a cage with only net six Lu-O nearest neighbors creating non-centrosymmetric subtle deformations in Fe^{3+}-O ligands.

These Fe^{3+} CF Zeeman branching in $LuFeO_3$ has as counterpart in the $ErFeO_3$ Er^{3+} ($^4I_{15/2}$) multiplet split strongly biased due to iron - rare earth exchanges. Er^{3+} ($^4I_{15/2}$) CF also overlaps with specific

lattice phonons suggesting conspicuous spin-phonon interactions appearing as an induced local continuum through the Er-O lattice vibrational range in the 1T/0T far infrared ratios. Weak applied fields are also enough to hint variants in partially magnetic-driven reststrahlen associated to torsional LO modes macroscopic fields involving moving Fe^{3+} ions.

While spin resonances under applied magnetic fields vary from characteristic enhancements to near CF degeneracies, we conclude that the overall complex setting, also undergoing some degree of lattice electric and magnetic coupling in a scenario prone to localized polaron formation, is likely common to all ferrite oxides.

SAMPLE PREPARATION AND STRUCTURAL CHARACTERIZATION

.

$RFeO_3$ (R= La, Pr, Er, Lu) polycrystalline samples were prepared by standard ceramic synthesis procedures. Stoichiometric amounts of analytical grade Fe_2O_3 and R_2O_3 powder oxides were thoroughly ground and heated in air at 1000ºC for 12 h and 1300ºC for 12 h in alumina crucibles. Then, pellets of ~1cm diameter, less than 2mm thick, were prepared by uniaxial pressing the raw powders and sintering the disks at 1300ºC for 2 h. The purity of the samples for all four $RFeO_3$ (R= La, Pr, Er, Lu) was checked by X-ray powder diffraction (XRD) collected at room temperature with Cu-Kα radiation. Shown in Fig. S3, all data were analyzed using the Rietveld method with refinements carried out with the program FULLPROF [49].

EXPERIMENTAL DETAILS

Low temperature-low frequency absorption measurements in the spectral range from 3 cm^{-1} to 50 cm^{-1} with 0.5 cm^{-1} resolution have been performed in the THz beamline of the BESSY II storage ring at the Helmholtz-Zentrum Berlin (HZB) in the low-alpha multi bunch hybrid mode. In the synchrotron low-alpha mode electrons are compressed within shorter bunches of only ~2 ps duration allowing far-infrared wave trains up to mW average power to overlap coherently in the THz range below 50 cm^{-1}. For measurements under magnetic fields, we used a superconducting magnet (Oxford Spectromag 4000, here up 7.5 T) interfaced with a Bruker IFS125 HR interferometer (Fig. S4). Temperatures were measured with a calibrated Cernox Sensor from LakeShore Cryotronics mounted to the copper block that holds the sample in the magnet Variable

Temperature Insert (VTI). Liquid helium cooled Si bolometers (4.2 K and 1.6 K from Infrared Labs) were used as detectors [49]. All measurements have been done in the Voigt configuration.

Far infrared near normal reflectivity spectra were taken on heating from 4 K to 300 K at 1 cm^{-1} resolution with a Bruker 113V and a Bruker 66 interferometers with conventional near normal incidence geometry. Samples were mounted on the cold finger of a He- closed cycle refrigerator and a home-made He cryostat adapted to the near normal reflectivity attachment vacuum chamber of the interferometer. He cooled bolometer and a deuterated triglycine sulfate pyroelectric bolometer (DTGS) were employed to completely cover the spectral range of interest. A plain gold mirror and in-situ evaporated gold film were used for 100% reference reflectivity between 4 K and 300 K. We analyzed the reflectivity spectra using the standard procedures for multioscillator dielectric simulation [49].

RESULTS AND DISCUSSION

a) $LaFeO_3$

Sharing the space group with the rest of $RFeO_3$ (R=lanthanide and Y) ferrites, four molecules per unit cell $LaFeO_3$ is the simplest compound that while closest to the cubic structure [50] still adopts the P_{bnm}-D_{2h}^{16} orthorhombic space group [51, 52**].**

$LaFeO_3$ G-type has spins coupled strongly antiferromagnetic below $T_N \sim 740$ K [53] in high spin configuration Fe^{3+} (half-filled $3D^5$) S=5/2. Inelastic neutron scattering spin wave intensities were found well represented by the Heisenberg exchange interaction between nearest neighbor antiferromagnetic planes prompting a van Hove singularity at ~ 564 cm^{-1} in the density of states spawning from 323 cm^{-1} to 630 cm^{-1} [54].

At lower frequencies, as pointed in the introduction, work on long wavelength spin waves has been mostly done under the umbrella of the so called two sublattice approximation [29] that considers spins 1-3 and 2-4 equivalent with each sublattice magnetization, M_1 and M_2, having its own equation of motion linked to the exchange interaction describing unequal precessions. The resonant energies then are given

$$\hbar|\omega_k^{\pm}| = g\mu_B\,[H_A\cdot(2\cdot H_E + H_A)^2]^{1/2} + g\mu_B H_0 \qquad (1)$$

where H_A=DS/gμ_B is the anisotropy field, H_E=2|J|zS/gμ_B (H_{Ei} = λM_i, i=1,2) with the exchange interaction J only for nearest neighbor spins, D is the exchange constant, S is the spin moment of the ith and jth nearest-neighbor metal transition ions and g is the gyromagnetic ratio as the spectroscopic splitting factor [56**].** A more quantitative treatment describing the THz active ferromagnetic and antiferromagnetic zone center spin wave resonances needs a full Hamiltonian incorporating anisotropies. The conventional spin Hamiltonian for orthorhombic ferrites [23, 24, 26, 33**]** is then written taking into account a single isotropic exchange constant coupling nearest neighbor transition metal spins, a single antisymmetric (canting) exchange constant, and two anisotropy constants as in

$$H_{spin} = 2 \cdot J \cdot \sum_{i,j} S_i \cdot S_j + \sum_{i,j} (D \cdot S_i \times S_j) + \sum_{i,j} \left(K_{eff} \cdot S_i\right)^2 \cdot \quad (2)$$

We thus expect a relative weak resonant long wavelength pair with near equal intensity, and comparable temperature and magnetic field dependences at near the Brioullin zone center. These are given by

$$\omega_{FM} = \{24 \cdot J \cdot S \cdot [2 \cdot (K_a - K_c) \cdot S]\}^{1/2} \quad (3)$$

$$\omega_{AFM} = \{24 \cdot J \cdot S \cdot [6 \cdot D \cdot S \cdot \tan\beta + 2 \cdot K_a \cdot S]\}^{1/2} \quad (4)$$

with the antiferromagnetic (ω_{AFM}) resonance at higher energies than the corresponding ferromagnetic (ω_{FM}), being J the exchange integral (J is positive for ferromagnets and negative for antiferromagnets) the isotropic Heisenberg constant and D the antisymmetric (DM) exchange, S is the spin moment of the ith and j^{th} nearest-neighbor metal transition ions, and K_a and K_c, are anisotropies along the ***a*** and ***c*** axes. β is the momentum canting angle off the ***ab*** plane [56**].**

Fig. 2 (a) shows the $LaFeO_3$ ferromagnetic (ω_{FM}) and antiferromagnetic (ω_{AFM}) zone center active resonances that, normalized by the absorption spectrum at 110 K, undergo a monotonous cooling down to 2.4 K. The lower and upper energy mode have frequency peaking at ω_{FM}=14.7 cm^{-1} and ω_{AFM}=20.1 cm^{-1} respectively. They are near temperature independent corroborating that by having La ($4f^0$) closed shell, avoiding extra potentially disturbing rare earth exchange, $LaFeO_3$ holds below T_N G-type magnetism in the Γ_4 (G_x, A_y, F_z) [53, 57-59**]** representation with canting angle α(deg.) ~0.52 [60**]** These resonances are found even in absence of an external field B_0, with

energies dependences fixed by exchange and anisotropy fields. We found that our peak positions are also in agreement with lower resolution inelastic neutron scattering measurements reporting broad features at those frequencies [61].

Applying an external field B_0, means that both modes will not longer remain degenerate since if one resonant mode is close parallel to the applied effective field the second has the opposite sign so that the resulting picture is a diverging split [29]. We find this behavior fully reproduced in our measurements of $LaFeO_3$ ferromagnetic- and antiferromagnetic-like modes as increasing applied field breaks their zone center degeneracy. This also reassures that our ZFC excitations have magnetic origin (Fig. S5).

We compute the induced modifications in zone center absorptions by the applied field B_0 by normalizing the measured spectra using the zero-field cooled (ZFC) run (Fig. 3). These ratios, (B_{0J}/0.0T), yield an absolute account of the field dependent spectral changes. The ω_{AFM} magnon initially peaks in intensity and remains unresolved up to about 3 T, meaning that this narrower band is result of two superposing excitations that remain unresolved at our working 0.5 cm^{-1} resolution. At higher fields it divides into two components. On the other hand, the ferromagnetic-like mode ω_{FM} shows only a gentle gradual splitting and broadening above 3 T. At 1T, Fig. S6**,** it may be further deconvoluted into two bands, a gaussian now centered at ~11.6 cm^{-1} and another much broader asymmetric at ~16.9 cm^{-1} with a truncated peak profile in the 1T-3T range, under a gaussian multiconstituent envelop, that may be understood as due to the disruption of individual magnetic sites by the external field. This resonance becomes narrower and comparable to the other magnetic bands increasing fields, all conforming under 7 T a close frequency quartet at 22.8, 21.3, 17.15 and 11.1 cm^{-1} (Fig. 3 (inset)) suggesting that the low fields broadening is consequence of precessing moments under inhomogeneous individual exchange and dampings excluded in the two-site picture. In this regard, it is also worth noting that the ZFC ω_{FM} mode at 14.7 cm^{-1} (Fig, S5-upper panel) has a band profile wide enough that may be also reproduced by two bands as for contemplating the existence of a zero field extra weaker intrinsic exchange. This, nonetheless, does not exclude considering the overall behavior of AFM- and FM-like magnons in $LaFeO_3$ be a suitable standard against the characterization shown in the following subsections for the $RFeO_3$ (R=Pr, Er, Lu) orthoferrites.

b) ***$PrFeO_3$***

Highly correlated non-Jahn-Teller $PrFeO_3$ is a Fe^{3+} high state distorted orthorhombic perovskite in which the A site rare-earth-oxygen distances embrace eight nearest neighbors out of the cubic twelve, (Fig. 1), conforming a sublattice in which the lanthanide $4f^2$ shell has CF $^3H_4$ ground state which multiplet crystal field splits into nine singlets.

This compound, as for $LaFeO_3$, is in the room temperature Γ_4 (G_x,A_y,F_z) magnetic representation below the Nèel temperature T_N ~703 K [62, 63]. It also develops below T_N weak ferromagnetism along the <u>c</u> axis due to Fe^{3+} canted moment with angle α(deg) =0.49◦.[57] On decreasing temperature, a broad inflexion in the reciprocal magnetic susceptibility has been associated to a spontaneous spin reorientation turning, between 201 K and 140 K, Γ_4 (G_x,A_y,F_z) into Γ_2 (F_x, C_y, G_z) rotating magnetic moments in the <u>*ac*</u> plane due to 4*f*-3*d* competing exchanges by Pr^{3+} and Fe^{3+} [20]. However, against this observation neutron diffraction patterns at 8 K confirm the G_x type antiferromagnetic arrangement. It also supports earlier conclusions by which weak Pr-Fe couplings question the possible reorientation phase transition [19].

We will assume that in our measurements the Γ_4 (G_x,A_y,F_z) representation holds in the temperature range of our studies.

At low temperatures we find a distinctive band at ~16.6 cm^{-1} that becomes sharper and that is also central to two much weaker and broader ones Fig.2(b). It softens, undergoing an energy down shift with zero field cooling from 5 K to ~2K, likely consequence of exchange couplings that without an apparent change in the side band profiles retain the high temperature magnetic representation Γ_4 (G_x,A_y,F_z). The central feature matches inelastic neutron data at 16 cm^{-1} (2.± 0.1 meV) assigned to the lowest of the 2J+1 $^3H_4$ ground state level, [65]. It has an asymmetric band shape reproduced by an overall Weibull profile due to its coalescing into near degeneracy with the bands at ~9.9 cm^{-1} and ~25.5 cm^{-1} contributing to the fused profile (Fig. S7). These last two are assigned to the ω_{AFM} and ω_{FM} modes by association with the resonances found in $LaFeO_3$ The emerging picture is close to what we earlier reported for $PrCrO_3$ where it was possible to deconvolute that main band into three components in spite that transition metal anisotropy fields together with the paramagnetic Pr^{3+} moments add random fluctuations in the AFM mode dynamically blurring magnetic oscillations [64]. In $PrFeO_3$ this would prevent well defined AFM

x,y out-of-phase and in-phase oscillations along the z axis and FM low frequency cones delineated by the ferromagnetic moment precessing the z axis (Fig. S2).

To have a better picture of the low energy spin dynamics, and possible field induced 3d-4f coupling along spin fluctuations, we also applied an external magnetic field. Fig. S8 shows that now, and as in $PrCrO_3$ [64**],** the lowest of the 2J+1 $3H_4$ ground state level behaves as expected for a 4*f* even electron lanthanide in ground crystal singlets being up to 7T nearly unaffected by the external field [66**].** There is, however, an effective weakening, broadening, and merging that may mask unresolved field weak dependences. As consequence, we only have significant departures from linearity in the broad feature assimilated to the ω_{FM} Fe^{3+} resonant mode. In either case, there is no field induced split degeneracy as found in $LaFeO_3$, but a field increase induced broadening suggesting that magnon splitting may be screened out due to the Pr^{3+} paramagnetism further disturbing magnetic couplings and anisotropies of the in-phase oscillation (ω_{AFM}) and precession (ω_{FM}) that in presence of the ground state dipole transition appear merging all excitations into one highly coupled mixed scenario**.** The relative clean profile for the ground level at weaker fields becomes a band with much less oscillator strength turning near featureless under 7.5 T at 5 K (Fig. 4). This is a likely consequence, again, of magneto dynamical fields in a mixed scenario in which the local microscopically altered lattice structure may play a role [67**].**

c) LuFeO₃

The magnetic dependent features found in $LaFeO_3$ are also expected for orthorhombic P_{bnm}-D_{2h}^{16} $LuFeO_3$ (T_N ~623 K) [68] since main differences in bulk properties are only introduced by the replacement of La by the also closed electronic shell Lu ($4f^{14}$). Both compounds, $LaFeO_3$ and $LuFeO_3$, share the Γ_4 (G_x, Ay, Fz) magnetic representation at room temperature [23] as well as canted ferromagnetism here with Fe^{3+} canting angle range α(deg.) =0.80◦ [17]- 0.61◦ **[**60**]** relative to the *a* oriented sublattice. As Lu^{3+} does not carry localized magnetic moment, it does not show neither magnetic compensation nor spin reorientation effects [69]. We find that for both compounds zero field cooled temperature dependences show profiles that may be assigned to magnons. For $LuFeO_3$ they are at ω_{FM} ~22.4 cm^{-1} and ω_{AFM} ~26.3 cm^{-1} (Fig. 2 (c)) with an extra third band at ~10.4 cm^{-1}. To understand this last one it is important to recognize that, in addition to rigid tilting and rotation, the consequence of Lu $4f^{14}$ smaller ionic radius at the A site is the edge

sharing inducing ligand distortions that indirectly trigger subtle changes in the octahedral FeO_6 B site. The changes in Fe-O bonding due to this ionic size dependence not only affects the known strong antiferromagnetic nearest neighbor Fe-O-Fe exchange interaction but also means a minute but effective local break in the space inversion symmetry allowing Fe^{3+} crystal field $^6A_1$ multiplet transitions. This slight perturbation at the B sites makes possible the detection of CF transitions and solves the puzzle on the appearance and nature of a third absorption in far infrared measurements by Aring and Sievers [70,71]. It also provides a clue of the lattice role on the origin of the ferroelectric loop in the magnetic ordered phase below $\sim T_N$ [**72].**

The effect introduced by lattice distortions due to smaller lanthanides in $RFeO_3$ has been recognized by phonon Raman scattering measurements [50**]** and it is most distinctive in changes in far infrared reflectivity when $LaFeO_3$ is compared against $LuFeO_3$.(Figs. S13-S16) Better defined bands, as for stretching modes around 600 $cm^{-1,}$ and the need of extra oscillators in fits (Tables SI-SIV) suggests minute energy differences translated into smaller ion displacements beyond most today's X-ray diffraction resolution and it is at the root of identifying ferroelectric spontaneous polarization in orthorhombic $LuFeO_3$ **[**73**].** It is also close to arguments on lattice strains as its possible origin in $RFeO_3$ thin films making plausible a $Pna2_1$ space group assignment rather than P_{bnm}**[**74**]** all compounding with the role played by the oxygen electronic polarizability in a ferroelectric phase transition.**[**75**]** The oxygen anisotropic volume dependent non-linear polarizability, that in ABO_3 introduces a dynamic covalent enhancing in the Oxygen p hybridization with Iron d states [76], allows a closer unified picture for ferroelectricity beyond introducing a foreign antisymmetric coupling of two non-equivalent spin pairs [77]. As it has been stressed many times most ferroelectrics are oxides where coexist displacive and order/disorder dynamics [78].

Fe^{3+} crystal field ground level transitions [79**]** for low level doped B sites in II- VI compounds are double degenerate and optically active in the lower THz portion of the spectra. They have been associated to transitions of the Fe^{3+} $^6A_1$ multiplet in embedded cage in the α-Al_2O_3 hematite-corundum lattice [80-82] when studying population inversion in Fe^{3+} doped sapphire [83-85]. We associate our local distortion at B sites with these "impurity" induced regimes in which the cubic pure symmetry turns into nearly Oh at distorted sites following the known concurrent structural sequence -cubic ($CaTiO_3$)-orthorhombic ($RFeO_3$)-rhombohedral (α-Fe_2O_3) [7].

Then the absorption band at ~10 cm^{-1}, Fig. 2 (c), and its linear Zeeman branching, (Figs. 5, S9) are interpreted as from the sextet Fe^{3+} $3d^5$ ($^6S_{5/2}$) in the octahedral crystal field under a subtle structural distortion [86]. The Fe^{3+} line in $LuFeO_3$ would be the highest Kramers degenerate level of the three expected to split linearly [81-83**].** It accounts for electron-electron repulsion, spin-orbit interaction, and crystal-field potentials [87-89].

The energy splitting under external magnetic fields allows to estimate the g factor using the linear relation,

$$\Delta E = \mu_B \, g \, B_0 \qquad (5)$$

that holds in the lower field regime. ΔE is the energy level Zeeman split shown in (Fig. 5 inset), μ_B denotes the Bohr magneton (μ_B=5.788 10-5 eV/T); g is a dimensionless constant, and B_0 the applied external magnetic field[90]. Our data at 5 K yields g_{net}=1.986 that, taking it as result from a close to four near inequivalent iron sites, coincides within the experimental error with g_e = 2.0023 for the free electron. It is the about value expected for high spin d^5 configuration as in transition metals like Fe^{3+}, meaning a very small orbital contribution to the magnetic moment (quenched orbital momentum) with negligible spin orbit coupling.

The lattice change may be also considered an intermediate step before further departing toward consolidating the hexagonal non-centrosymmetry non-perovskite arrangement. This is a metastable hexagonal structural configuration described by the polar P63cm space group , as in H-$LuFeO_3$, where a trivalent transition metal ion occupies a trigonal bipyramidal site (RO_5) [91, 92] rendering the view that low level A-site substitutions in ABO_3 compounds are functional to weak ferroelectricity [93].

As pointed, at slightly higher frequencies than the Fe^{3+} ground transition the two zone center resonant magnon modes, ω_{FM} and ω_{AFM}, are found in zero field cooled runs at ~22.4 cm^{-1} and ~26.3 cm^{-1} respectively. Peak positions suggest a behavior equivalent to those in $LaFeO_3$ and are in agreement with an earlier peak quotation by Aring and Sievers [70]**.** However**,** in $LuFeO_3$ both resonances under applied fields (peripherical insets in Fig. S10) seem linked by a strong "bridge" that it is only reproduced in fits by introducing an extra background band with distinctive increasing asymmetry. They evenly diverge out the center frame under increasing fields. Herrman [23] pointed out that when considering the four Fe^{3+} magnetic sites, rather than the two sublattice

model, it is necessary to take into account not only the so called plain "overt" canting but also a hidden canting mechanism producing no net magnetization. It was found that this last mechanism is particularly significant for the case when the antisymmetric exchange is smaller than the anisotropy energy (A>>D), a case suggested by our $RFeO_3$ (R=rare earth) measurements. We may then conjecture that the optical activity of the bridging excitation at frequencies between the FM and AFM modes is due to an unresolved constituent of hidden canting inducing coupling between exchange and magnon resonances. The exchange resonances by themselves are expected to be optically inactive in antiferromagnetics.[23]

We also observe at intermediate frequencies that there is a weaker quasi-undulating pattern composed by emerging four maxima where Fe^{3+} branch meets the diverging FM magnon,. Zooming in the 15 cm^{-1} to 20 cm-^{1} window, Fig. S10 (arrow at 1T), becomes apparent that they may be reproduced by partial superposition of two broad Gaussians (for simplicity the remaining three are omitted). They amount to four individual peaks field induced as from inequivalent magnetic four sites beyond the two site hypothesis. This frequency spread also appears on the higher frequency branching of the ω_{AFM} mode (Fig. S11) that, while still following the main frame up to 7 T, suggests both resonances tangled in a more collective complex trend blurring individual phase motions consequence of the same lattice perturbation that , causing Fe^{3+} optical activity, may be thought at the root of single ion anisotropy as for the origin of spin canting [1**7**]**.**

d) ***ErFeO₃***

$ErFeO_3$ (T_N ~633 K) [30, 53**]** orthorhombic P_{bnm}-D_{2h}^{16} is perhaps one the most study compound of the ferrite family [94**].** Starting at about 220 K and on cooling [95] Er^{3+} moments start forcing the prevailing magnetic oriented iron moments in the Γ_4 (G_x, F_z) representation to rotate in 90° into the F_2 (G_z ,F_x) *a*-axis alignment in an interval from T_1= 87 K (90 K) to T_2=96.6 K (103 K). [97,98]**.** This mostly magnetic displacive phase transition, in which has also been reported strong spin-lattice coupling, is common to canted ferromagnetism in all partially filled rare earth *f*-odd shell compounds [8, 30**,** 98-101**].**

We studied in this Γ_2(G_z , F_x) phase the Fe^{3+} ($^6A_1$) and the Er^{3+} ($^4I_{15/2}$) manifolds as well as the two spin resonances. As it is shown in Fig. 6, the Fe^{3+}($^6A_1$) transition, extrapolated in our detection limit to ~4 cm^{-1} , undergoes a linear Zeeman split in a perturbed A site close behaving

the discussed in the section for $LuFeO_3$. However, unlike the symmetric profile in $LuFeO_3$ (Fig. 5), it is now biased toward higher energies due to a drift associated to the Er^{3+}-Fe^{3+} magnetic exchange.

The FM and AFM resonances at ω_{FM}~21.5 cm^{-1} and ω_{AFM}~ 31.5 cm^{-1} have an equally weak field dependences up to the compensation temperature T_{CMP} [102]. This is the temperature at which the antiferrogamentic exchange interaction of paramagnetic Er^{3+} moment equals the near constant moment of Fe^{3+} spins meaning a net polarization of the Er^{3+} spins antiparallel to the canted Fe^{3+} [103]. That is, the negative exchange interaction of the iron and erbium yields a total spontaneous moment written as

$$M=M_0 + \chi_R \cdot H_0 \qquad (6)$$

being M_0 the ferromagnetic moment, χ_R the paramagnetic rare earth susceptibility, and H_0 the exchange field at the rare earth by the irons. With negative exchange interaction the rare earth induced magnetic moment decreases and so the total magnetic moment diminishes up to vanishing at T_{CMP} [104]. A vanishing point also remains upon applying an external magnetic field such that at temperatures above it the canted ferromagnetism is directed along the field.

Fig. 7 (a) shows that on cooling the intensity of the AFM resonance increases continuously below the reorientation temperature T_{RS} peaking at about 5 K to then turning into a sharp decrease as $ErFeO_3$ gets closer to the Γ_1 (A_x, G_y, C_z) phase. In this phase, after softening, it merges with the much weaker hardening ferromagnetic mode (ω_{FM}). This results in a single much broad feature characteristic of Γ_1 phase as the Fe^{3+} spins undergo a gradual G_z to G_y rotation due Er^{3+} exchange coupling leading to cooperative antiferromagnetic for Er^{3+} below T_N(Er) ~4.5 K. (Fig. 7 (a,b)) This behavior is similar to what has been reported for $ErCrO_3$ in the same temperature range [64].**]**. The sharp decrease of the ω_{AFM} mode intensity signals the onset of the $G_{xy}F_x$ mixed spin arrangement [102] at the time that corresponding magnetic structure turns into fully C_z antiferromagnetic oriented for Er^{3+} and magnetic $C_yG_zF_x$ for Fe^{3+} [107,108] in a potential low temperature monoclinic space group $P_{21/m}$.

$ErFeO_3$ field induced absorptions using as reference the ZFC spectrum are shown at 5 K in Fig. 8. As it was in their temperature dependence, the induced change at the AFM resonance undergoes a

huge enhancement while the rather weak FM mode behave accordingly to the previous cases. However, at difference with what we found for the other compounds they do not diverge split upon applying up to 7 T. It appears as if their divergency is compensated by the Fe^{3+}-Er^{3+} exchange yielding a very narrow picture that, unsolved at our working resolution, increases in intensity as assuming superposing two gaussians.

Zero field ratios calculated using the spectra taken for the initial and after the 7 T run yield extra absorptions at both magnons frequencies bringing up the delicate nature of the exchange on these modes. Interpreted as a memory effect this behavior may also help to explain the origin of the broad and intriguing extra line reported by Mikhaylovskiy et al [105]. Our spectra show that at zero field the Fe^{3+} unfolded multiplet and zone center magnons are separated by at least 15 cm^{-1} thus ruling out an interference as a possible explanation. Rather, the unexplained extra band shouldering the ferromagnetic mode might have been created by a laser induced distortion changing locally the effective temperature within the dynamics of the resonant mode.

Alongside the temperature dependent-field dependent changes of the magnetic resonances, the overall picture for the Fe^{3+} and Er^{3+} multiplet transitions remain essentially unaltered (Fig. S12). We note, however, that bands of the Zeeman Fe^{3+} lower energy branch associated to intensity increments, at increasing field ratios, correspond to a shallow response in the branch facing the Er^{3+} ($^4I_{15/2}$) Zeeman split at higher frequency. Only when ratios for this last one are calculated decreasing fields we retrieve meaningful gaussian profiles (blue traces in Figs.9-S12) suggesting depopulated levels due to Er^{3+} exchange. The applied field disrupts selectively the known symmetric part of the exchange energy between the two Fe^{3+} magnetic sublattices S_i and S_j and thus the zero field superexchange involving nearest neighbors Fe+ ions via intermediate O^{-2} ion. In zero field superexchange one spin up electron virtually hops to oxygen forming an up-down pair and back to the same spin orientation [106]. We find that this mechanism is particularly sensible to the paramagnetic Er^{3+} lowest Zeeman branch when the higher Fe^{3+} and lower Er^{3+}, branches meet at T_{CMP} ~40 K at about 30 cm^{-1} and ~5 T (solid arrow in Fig. 6). In this scenario, and in contrast with the clean picture suggested by the $LuFeO_3$ analysis, the calculation of the g factor now reflects increasing couplings and anisotropies induced by the ligand field in what would imply an net effective result. Choosing energy levels at intermediate fields from the skew Zeeman split shown in fig. 9(a) and replacing B_0 by $B_{eff} = (B_0 + B_{local})$ and g by g_{eff} in eq (5) [90] we found B_{local} ~1.08 T that in turn results in a ballpark $g_{eff} \sim 10.0 \pm 0.5$.

While there is Fe^{3+} ($^6A_1$) population inversion at all temperatures, in the Er^{3+} branch it is only associated to paramagnetic Er^{3+} random dipoles. In $ErFeO_3$ the field dependent extra absorption at 40 K about 30 cm^{-1} and ~5 T diminishes as Er^{3+} gets closer to its ordered antiferromagnetic phase where branching becomes near field independent. At 5 K the induced change becomes undetectable and at 2.4 K has totally disappeared allowing undistorted Gaussian profiles in the Fe^{3+} ($^6A_1$) higher frequency branch (Figs.9(b)-S12).

e) Er^{3+} multiplet and phonon field dependences

To get a full view of the temperature field dependence of the Er^{3+} ($^4I_{15/2}$) multiplet it is necessary to run far infrared spectra. In this range the near normal reflectivity of $ErFeO_3$ at 5K, Fig. S14, is dominated by phonon profiles that may be broadly grouped into a lower frequency region centered at ~ 200 cm^{-1} for lattice vibrations in which the rare earth moves against FeO_6 sublattice, a second one centered ~350 cm^{-1} that it is characterized by Fe scissor and stretching modes as well as octahedral librations, and a third one for oxygen breathing-stretching-modes at ~600 cm^{-1}. When this reflectivity is matched to the absorption ratio of 1 T against 0 T spectra, Fig. 10 (a), it is straight forward to locate the Er^{3+} ($4f^{11}$) three Kramers ($^4I_{15/2}$) doublets as their magnetic signature appears at 49.5 cm^{-1} (6.14 meV), 110.5 cm^{-1} (13.7 meV) and 167.3 cm^{-1} (20.74 meV). They are in agreement with recent inelastic neutron scattering measurements [108], and earlier estimates [110].

Just 0.5 T is enough to lift the Er^{3+} Kramer degeneracy by ~5 cm^{-1} (0.62 meV) into two weaker bands. At temperatures below compensation point T_{cmp}~40 K, and increasing the fields, Fig. 11, they turn into strong asymmetric Zeeman splits correlated with the Fe^{3+} branching at lower frequencies. While this asymmetric picture is seen for the three transitions, it is particularly clear for the third level at 167.3 cm^{-1} being symmetric above T_{cmp} to then have a field insensitive lower frequency branch as it becomes associated to the Fe^{3+} exchange at and below T_{cmp} (Fig. S17).

Er^{3+} levels at 110.5 cm^{-1} and 167.3 cm^{-1} fall at known reflectivity phonon frequencies for vibrational modes involving rare-earth displacements and, least for one case, seems to be also related to an A_g phonon in Raman spectra that for $LaFeO_3$ is at 84.5 cm^{-1}[50**].** Fig. 10 (a) also shows a dotted line across a continuous envelop in the field induced absorption of the 1 T/ 0 T

ratio coinciding with the region of external lattice vibrations. It suggests localized charge delocalization for the frequencies where phonons are found interacting with the crystal field levels and thus spins.

Next, at increasing frequencies, there are three individual field enhancements centered at ~400 cm^{-1}, the frequency for Fe^{3+} torsional vibrations (vertical arrows in Fig. 10(a)). Each phonon corresponds to a field induced absorption that becomes stronger at frequencies closer to the respective longitudinal optical mode associated to the reflectivity transverse optical-longitudinal optical (TO-LO) restrahlen split. As it is shown in Fig. S14 under 1T we do not find a magnetic response for breathing stretching modes centered at ~600 cm^{-1} where only oxygens move. Field dependences are only detected for vibrations involving moving magnetic ions, in our case Er^{3+} and Fe^{3+}, fulfilling the basic premise in TO-LO magnetoelectrics by which ion displacements couple electric and magnetic contributions appearing in the macroscopic field [9**].** This contrasts with dielectric insulators where macroscopic field linked to a longitudinal optical mode is only associated to long-range electric fields as restoring force due to Coulomb interactions and by which LO frequency is a minimum over its restrahlen [10**].**

Conclusions

Summarizing, we studied low temperature-low energy absorptions of $LaFeO_3$ antiferromagnetic and ferromagnetic magnons at ω_{FM} ~26.7 cm^{-1} and ω_{AFM} ~31.4 cm^{-1} in the Γ_4 (G_x, A_y, F_z) representation. We found that their degeneracy is lifted about linearly by an applied fields up to 7 T. In isomorph $LuFeO_3$ in addition to these two spin modes, now peaking at ω_{FM} ~22.4 cm^{-1} and ω_{AMF} ~26.3 cm^{-1}, there is a Fe^{3+} crystal field $^6A_1$ transition at ~10.4 cm^{-1} which activity is tied to ligand distortions induced by Lu^{3+} $4f^{14}$ smaller ionic radius. This A site deformation triggers subtle lattice changes at the perovskite B site and allows a linear Zeeman split up to 7 T. It is also found in $ErFeO_3$ (Kramers $4f^{11}$ Er^{3+}; Γ_2 (F_x, C_y, G_z) $<T_{SR}$ ~93 K), where now the Fe^{3+} Zeeman branching is strongly biased toward higher energies due to 3d-4f exchange. Within our 0.5 cm^{-1} working resolution at 5 K, and in contrast with magnons in $RFeO_3$ (R=La, Lu), there is no field induced splits but a low temperature 13-fold increase in the intensity of the resonance antiferro/ferro mode ratio. It is also remarkable the CF matching population balance between Fe^{3+} higher and Er^{3+} lower Zeeman-split branches.

Er^{3+} ($^4I_{15/2}$) transition energies from the ground multiplet at 110.5 cm^{-1} and 167.3 cm^{-1} coincide with external lattice mode frequencies suggesting strong crystal field-phonon couplings in a scenario for lattice driven spin-phonon interactions. Absorption spectra ratios under mild external fields reveal a magnetic dependent local quasi-continuum in the Er-O vibrational region and enhancement in longitudinal optical mode macroscopic fields associated to Fe^{3+} torsional modes, i.e., field dependences are only detected for vibrations involving moving magnetic ions.

Antiferro- and ferro- resonances turn in $PrFeO_3$ much broader when non-Kramers Pr^{3+}, with two unpaired $4f^2$ electrons, introduces ligand changes at the A site leading the ω_{AFM} mode and the lowest Pr^{3+} CF transition into near degeneracy. This and the ω_{FM} merge at 7 T into a single broad mostly unresolved feature.

We conclude that low energy excitations in $RFeO_3$ (R=rare earth) strongly depend on the lanthanide ionic size thus indivisibly tied to the mechanism associated to the origin of canted ferromagnetism. Minute lattice displacements in the perovskite basic BO_6 and AO_{12} building blocks also underlies the fact that the ferroelectric instabilities might already be present above Tc at sites with thermal distribution of the ionic motion. Peaking at actual centrosymmetric sites may really be due to some multi-well configuration as most ferroelectrics appear to be in the middle ground represented by shallow double wells and anharmonic rough single wells.[111] This argument motivates the possibility of assigning non-centrosymmetry to those distorted perovskites with smaller rare earth ionic radius as for the P*na2₁* space group. I.e., with Fe^{3+} not at a center of inversion in a rigid ion approximation. Then, it is necessary to also take into account the hybridization between oxygen p and transition-metal d electrons. As a feature in driving the ferroelectric instability, it will dynamically enhance the oxygen volume dependent electronic polarizability that it is tied to the emergence of the weak spontaneous polarization within the framework of most known ferroelectric oxides [78, 111].

Acknowledgements

The authors are pleased to acknowledge the enlightening insights and full support at the THz beamline by K. Holldack (Department Optics & Beamlines, Helmholtz-Zentrum für Materialien und Energie GmbH (HZB), D-12489) during the development of the present work. NEM is indebted to BESSYII at the Helmholtz-Zentrum Berlin für Materialien und Energie for beamtime allocation under proposals 201-09204-ST, 202-09707-ST, 212-10296-ST, 221-10915-ST, 221-10941-ST, 222-11422-ST and 222-11426-ST and for financial assistance supported by the project CALIPSO plus under the Grant Agreement 730872 from the European Union Framework Program for Research and Innovation HORIZON 2020. He also thanks the laboratory on Conditions Extrêmes et Matériaux: Haute Température et Irradiation - UPR3079 CNRS (C.E.M.H.T.I.)) in Orléans and the Groupement de Recherche Matériaux Microélectronique Acoustique Nanotechnologies (GREMAN-UMR7347)-Université François Rabelais Tours, for sharing expertise on research and financial support performing far infrared reflectivity measurements. JAA acknowledges the ILL-Grenoble for the allowed neutron time, and the financial support of the Spanish Ministry for Science and Innovation (MCIN/AEI/10.13039/501100011033) for granting the project number: PID2021-122477OB-I00-R.

References

1. M. Fiebig, T. Lottermoser, D. Meier and M. Trassin, The evolution of multiferroics, Nat. Rev. Mater **1**, 16046 (2016).
2. N. A. Spaldin and M. Fiebig, The Renaissance of Magnetoelectric Multiferroics,Science **309**, 391 (2005).
3. N. D. Todorov, M. V. Abrashev, and V. G. Ivanov, Frequency dependence of the quasi-soft Raman-active modes in rotationally distorted $R^{3+}B^{3+}O_3$ perovskites (R^{3+}= rare earth, B^{3+} = Al, Sc, Ti, V, Cr, Mn, Fe, Co, Ni, Ga), J. Phys.: Condens. Matter 24 175404 (2012).
4. H. Forestier and G. Guiot-Guillain, Une nouvelle série de corps ferromagnetiques: les ferrites de terres rare, Compt. Rend. 230, 1844 (1950).
5. D. Treves, Studies on Orthoferrites at the Weizmann Institute of Science, J. of Appl. Phys. **36**, 1033 (1965).
6. R. L. White, Review of Recent Work on the Magnetic and Spectroscopic Properties of the Rare-Earth, J. of Appl. Phys. **40**, 1061 (1969).
7. Magment GmbH, Germany; https://www.magment.co/
8. R. Resta, Lyddane-Sachs-Teller Relationship in Linear Magnetoelectrics Phys. Rev. Lett. **106**, 047202 (2011).
9. P. Yu and M. Cardona, Fundamentals of Semiconductors, 2nd ed, chapter III, Springer-Verlag, Berlin (1999).
10. S. M. Shapiro, J. D. Axe, and J. P. Remeika, Neutron-scattering studies of spin waves in rare-earth orthoferrites, Phys. Rev. B **10**, 2014 (1974).
11. M. Marezio, J. P. Remeika, and P. D. Dernier, The Crystal Chemistry of the Rare Earth Orthoferrites, Acta Cryst. B**26**, 2008 (1970).
12. D. J. Lam, B. W. Veal, and D. E. Ellis, Electronic structure of lanthanum perovskites with 3d transition elements, Phys. Rev. B **22**, 5730 (1980).
13. E. F. Bertaut, in "Magnetism: A Treatise on Modern Theory and materials" G.T. Rado and H. Suhl, eds., Vol. 3,p.149, Academic Press, New York (1963).
14. F. Bertaut and F. Forrat, Structure des Ferrites Ferrimagnétiques des Terres Rares, C.R. Acad.Sci. (Paris) **242**, 382 (1956)**.**

15. T. Yamaguchi, Theory of Spin Reorientation in Rare-earth Orthochromites and Orthoferrites, J. Phys. Chem. Solids **35**, 479 (1974).
16. A. Moskvin , Dzyalonshinkii,-Moriya Coupling in 3d Insulators, Condens. Matter**. 4**, 84 (2019)
17. J.-S. Zhou, L. G. Marshall, Z.-Y. Li, X. Li, and J.-M. He Weak ferromagnetism in perovskite oxides Phys. Rev. B **102**, 104420 (2020).
18. H. Homer and C. M. Varma, Nature of Spin-reorientation Transitions, Phys. Rev. Lett. **20,** 845 (1968).
19. P. Pataud and J. Sivardière, Chaleurs Spécifiques a Basse Température de Quelques Orthoferrites et Orthochromites de Terres Rares, J. de Physique **31,** 1017 (1976).
20. Z. Zhou, L. Guo, H. Yang, Q. Liu, F. Ye, Hydrothermal Synthesis and Magnetic Properties of Multiferroic Rare-earth Orthoferrites, J. Alloys Compd. **583** 21 (2014).
21. K. P. Belov, A. K. Zvezdin and A. M. Kadomtseva, Sov. Sci. Rev. Sect. A. Phys. **9**, 117 (1987).
22. C. H. Tsang, R. L. White and R. M. White, Spin wave damping of domain walls in $YFeO_3$, J. of Appl. Phys. **49**, 6063 (1978).
23. G. F. Herrmann, Magnetic Resonances and Susceptibility in Orthoferrites, Phys. Rev. **133,** A1334 (1964).
24. G. F. Herrmann, Resonance and high frequency susceptibility in canted antiferromagnetic substances, J.. Phys. Chem. Solids **24**, 597 (1963)).
25. C. H. Tsang, R. L. White and R. M. White, Spin wave damping of domain walls in $YFeO_3$, J. of Appl. Phys. **49**, 6063 (1978).
26. R. M. White, R. J. Nemanich, and C. Herring, Light scattering from magnetic excitations in orthoferrites, Phys. Rev. B **25**, 1822 (1982).
27. C. Kittel, Theory of Antiferromagnetic Resonance, Phys. Rev. **82**, 565 (1951).
28. T. Nagamiya, Theory of Antiferromagnetism and Antiferromagnetic Resonance Absorption, Progress of Theoretical Physics **6**, 342 (1951).
29. F. Keffer, and C. Kittel, Theory of Antiferromagnetic Resonances Phys. Rev. **85**, 329 (1952).
30. N. Koshizuka and S. Ushioda, Inelastic-light-scattering study of magnon softening in $ErFeO_3$, Phys. Rev. B **22**, 5394 (1980).

31. N. Koshizuka, and K Hayashi, Raman Scattering from Magnon Excitations in $RFeO_3$, J. Phys. Soc. Jpn. **57**,. 4418 (1988).
32. G. V. Koslov, S. P. Lebedev, A. A. Mukhr, A. S. Prokhorov,and L. V. Fedorov Submillimeter backward-wave oscillator spectroscopy of the rare-earth orthoferrites IEEE Trans. on Magnetics **29** 3443 (1993).
33. E. Constable , D. L. Cortie, J. Horvat, R. A. Lewis, Z. Cheng, G. Deng, S. Cao, S. Yuan, and G. Ma, Complementary terahertz absorption and inelastic neutron study of the dynamic anisotropy contribution to zone-center spin waves in a canted antiferromagnet NdFeO3 Phys. Rev. B **90**, 054413 (2014).
34. J Jiang, Z Jin, G Song, X Lin, and G. Ma, Dynamical Spin Reorientation Transition in $NdFeO_3$ Single Crystal Observed with Polarized Terahertz Time Domain Spectroscopy, Appl. Phys. Lett. **103**, 062403 (2013).
35. X. Fu, X. Zeng, D. Wang, H. Chi-Zhang, J. Han, and T. J. Cui, Ultralow temperature terahertz magnetic thermodynamics of perovskite-like $SmFeO_3$ ceramic Sci. Rep. **5**, 14777; 10.1038/srep14777 (2015).
36. K. Zhang, K. Xu, X. Liu, Z. Zhang, Z. Jin, X. Lin, B. Li., S. Cao, and G. Ma, Resolving the spin reorientation and crystal-field transitions in $TmFeO_3$ Sci Rep **6**, 23648 (2016).
37. K. Amelin, U. Nagel, R. S. Fishman, Y. Yoshida, Hasung Sim, Kisoo Park, Je-Geun Park, and T. Rõõm, Terahertz Absorption Spectroscopy Study of Spin Waves in Orthoferrite $YFeO_3$ in a Magnetic Field, Phys. Rev. B **98,** 174417 (2018).
38. X Li, M. Bamba, N. Yuan4, Q. Zhang, Y. Zhao, M. Xiang, K. Xu, Z. Jin, W. Ren, G. Ma, S. Cao, D. Turchinovich, J. Kono, Observation of Dicke cooperativity in magnetic interactions, Science **361**, 794 (2018).
39. S. A. Skorobogatov, S. E. Nikitin, K. A. Shaykhutdinov, A. D. Balaev, K. Yu. Terentjev, G. Ehlers, G. Sala, E. V. Pomjakushina, K. Conder, and A. Podlesnyak Low-temperature spin dynamics in the $TmFeO_3$ orthoferrite with a non-Kramers ion Phys. Rev. B 101, 014432 (2020).
40. S. A. Skorobogatov, K. A. Shaykhutdinov, D. A. Balaev, M. S. Pavlovskii, A. A. Krasikov,and K. Yu. Terentjev Spin dynamics and exchange interaction in orthoferrite TbFeO3 with non-Kramers rare-earth ion arXiv.2204.03239).

41. R.D. Shannon and C.T. Prewitt, Effective Ionic Radii in Oxides and Fluorides, Acta Cryst. B**25**, 925 (1969).
42. R. D. Shannon, Revised Effective Ionic Radii and Systematic Studies of Interatomie Distances in Halides and Chaleogenides, Acta Cryst. A**32**, 751 (1976).
43. (I. S. Lyubutin, T. V. Dmitrieva, and A. S. Stepin, Dependence of exchange interactions on chemical bond angle in a structural series:cubic perovskite–rhombic orthoferrite–rhombohedral hematite, (Zh. Eksp. Teor. Fiz. **115**, 1070 (1999))- J. Exp. Theor. Phys. 88 590 (1999).
44. J.-S. Zhou and J. B. Goodenough, Intrinsic structural distortion in orthorhombic perovskite oxides, Phys. Rev. B **77**, 132104 (2008)
45. J.-S. Zhou and J. B. Goodenough, Universal Octahedral-Site Distortion in Orthorhombic Perovskite Oxides, Phys. Rev. Lett. **94**, 065501 (2005).
46. J. A. Alonso, M. J. Martínez-Lope, M. T. Casais, and M. T. Fernández-Díaz, Evolution of the Jahn−Teller Distortion of MnO_6 Octahedra in $RMnO_3$ Perovskites (R = Pr, Nd, Dy, Tb, Ho, Er, Y): A Neutron Diffraction Study, Inorg. Chem. **39**, 917 (2000).
47. J.-S. Zhou, J.A. Alonso, V. Pomjakushin, J.B. Goodenough, Y. Ren, J.-Q. Yan, and J.-G. Cheng, Intrinsic structural distortion and superexchange interaction in the orthorhombic rare-earth perovskites $RCrO_3$, Phys. Rev. B **81**, 214115 (2010).
48. S-J Kim, G. Demazeau, I. Presniakov and J-H Choy, Structural Distortion and Chemical Bonding in $TlFeO_3$: Comparison with $AFeO_3$ (A=Rare Earth), J. of Sol Stat Chem 161, 197 (2001).
49. Supplemental Material (information on sample preparation, X-ray diffractograms, and magnetic characterization; layout of the THz beamline at BESSY II; $RFeO_3$ (R=La,Er,Lu) far infrared data and multioscillator fits; temperature dependence of Fe^{3+} ($^6A_1$) and Er^{3+} ($^4I_{15/2}$) CF Zeeman and magnons from 110 K to 2.4 K in $ErFeO_3$; $ErFeO_3$ far infrared Er^{3+} ($^4I_{15/2}$) Zeeman multiplet biased due to Fe^{3+} ($^6A_1$) exchange from 75 K to 2.3 K.
50. M. C. Weber, M. Guennou, H. J. Zhao, J. Íñiguez, R. Vilarinho, A. Almeida, J. A. Moreira, and J. Kreisel, Raman spectroscopy of rare-earth orthoferrites $RFeO_3$ (R=La, Sm, Eu, Gd, Tb, Dy), Phys. Rev. B **94**, 214103 (2016).

51. S. Geller and E. A. Wood, Crystallographic studies of perovskite-like compounds. I. Rare earth orthoferrites and $YFeO_3$, $YCrO_3$, $YAlO_3$, Acta Crystallogr. **9**, 563 (1956),
52. M. Marezio and P. D. Dernier, The bond lengths in $LaFeO_3$, Materials Research Bulletin **6**, 23 (1971).
53. W. C. Koehler, E. O. Wollan, and M. K. Wilkinson, Neutron-diffraction study of the magnetic properties of Rare Earth Iron Perovskites, Phys. Rev. **118**, 58 (1960).
54. R. J. McQueeney, J.-Q. Yan, S. Chang, and J. Ma, Determination of the exchange anisotropy in perovskite antiferromagnets using powder inelastic neutron scattering, Phys. Rev. B **78**, 184417 (2008).
55. K. Yosida, "Theory of Magnetism," Springer Series in Solid-State Sciences, Vol. 122, 2010, Chap. 9
56. M. Eibschütz, S. Shtrikman, and D. Treves, Mössbauer Studies of Fe^{57} in Orthoferrites, Phys. Rev. **156**, 562 (1967).
57. S. Stolen, F. Gronvold, H. Brinks, T. Atake, and H. Mori, Heat capacity and thermodynamic properties of $LaFeO_3$ and $LaCoO_3$ from T = 13 K to T = 1000 K, J. of Chem. Thermodyn. **30**, 365 (1998).
58. S.C. Parida, S.K. Rakshit, and Z. Singh, Heat capacities, order–disorder transitions, and thermodynamic properties of rare-earth orthoferrites and rare-earth iron garnets J. Solid State Chem. **181,** 101 (2008).
59. S. M. Selbach, J. R. Tolchard, A. Fossdal, and T. Grande, Non-linear thermal evolution of the crystal structure and phase transitions of $LaFeO_3$ investigated by high tenmperature X-ray diffraction, J. of Solid State Chem. **196**, 249 (2012).
60. T. Fujii, I. Matsusue, and J. Takada, in Advanced Aspects of Spectroscopy, ed. M. A. Farrukh, chap. 13 pp. 373–390. InTech (2012).
61. K. Park, H. Sim, J. C. Leiner,Y. Yoshida, J. Jeong, S-I. Yano, J. Gardner, P. Bourges, M. Klicpera,V. Sechovský, M. Boehm and J-G. Park, Low-energy spin dynamics of orthoferrites $AFeO_3$ (A = Y, La, Bi), J. Phys.: Condens. Matter **30,** 235802 (2018).
62. I Sosnowska and P Fischer, Refinement of the crystal and magnetic structure of $PrFeO_3$ AT T = 8 K, J. of Less Common Met. **111** 109 (1985).
63. Y. Nagata, S. Yashiro, T. Mits uhashi, A. Koriyama, Y. Kawashima, H. Samata, Magnetic properties of $RFe_{1-x}Mn_xO_3$ (R=Pr, Gd, Dy), J. Magn. Magn. Mater. **237** 250 (2001).

64. N. E. Massa, K. Holldack, R. Sopracase, V. Ta Phuocc, L. del Campo, P. Echegut, and J. A. Alonso, Identification of spin wave resonances and crystal field levels in simple chromites $RCrO_3$ (R = Pr, Sm, Er) at low temperatures in the THz spectral region, J. Magn. Magn. Mat. **468,** 294 (2018).
65. K . Feldmann, K. Hennig, L. Kaun, B . Lippold, M. M. Lukina, S. Matthies, W. Matz, and E. Warming Crystal field levels of Pr^{3+} in $PrFeO_3$ and $PrGaO_3$ determined by inelastic neutron scattering **72** 817 (1975).
66. A. P. Malozemoff and R. L.White, Optical spectra of even-electron rare earth ions in the orthoferrites, Sol. St. Comm. **8** 665 (1970).
67. J. Cao, L. I. Vergara, J. L. Musfeldt, A. P. Litvinchuk, Y. J. Wang, S. Park, and S.-W. Cheong, Spin-Lattice Interactions Mediated by Magnetic Field, Phys. Rev. Lett. **100**, 177205 (2008).
68. N. P. Cheremisinoff, Handbook of Ceramics and Composites, Taylor & Francis, New York (1990).
69. A. Bombik, H. Böhm, J. Kusz and A. W. Pacyna, Spontaneous magnetostriction and thermal expansibility of $TmFeO_3$ and $LuFeO_3$ rare earth orthoferrites, J. Magn. Magn. Mater. **234,** 443 (2001).
70. K. B. Aring and A. J. Sievers, Role of the Ytterbium Spins in the Spin Reorientation in $YbFeO_3$, J. of Appl. Phys. **41**, 1197 (1970)).
71. S. Venugopalan and M. M. Becker, Raman scattering study of $LuFeO_3$, J. Chem. Phys. **93**, 3833 (1990).
72. N. M. Kovtun, A. S. Karnachev, E. E. Soloviev, A. Y. Chevonenkis, and Shemyakov, NMR study of spin reorientation in $ErFeO_3$ weak ferromagnet. Fiz. Tverd. Tela (Leningrad) **14**, 2150 (1972); [Sov. Phys. Solid State **14**, 1856 (1973)].
73. U. Chowdhury, S. Goswami, A. Roy, S. Rajput, A. K. Mall, R. Gupta, S. D. Kaushik, V. Siruguri, S. Saravanakumar, S. Israel, R. Saravanan, A. Senyshyn, T. Chatterji, J. F. Scott, A. Garg, and D. Bhattacharya, Origin of ferroelectricity in orthorhombic $LuFeO_3$, Phys. Rev. B **100**, 195116 (2019).
74. H. J. Zhao, Y. Yang, W. Ren, A-J Mao, X. M. Chen and L. Bellaiche, Creating multiferroics with large tunable electrical polarization from paraelectric rare-earth orthoferrites, *J. Phys.: Condens. Matter* **26**, 472201 (2014).

75. H.Bilz, G.Benedek, and A. Bussmann-Holder, Theory of ferroelectricity: The polarizability model Phys. Rev. B **35** 4840 (1987).
76. R. Migoni, H. Bilz, and D. Bäuerle, Origin of Raman Scattering and Ferroelectricity in Oxidic Perovskites, Phys. Rev. Lett. **37**, 1155 (1976).
77. H. Katsura, N. Nagaosa, and A. V. Balatsky, Spin Current and Magnetoelectric Effect in Noncollinear Magnets., Phys. Rev. Lett. **95**, 057205 (2005).
78. A. Bussmann-Holder The polarizability model for ferroelectricity in perovskite oxides *J. Phys.: Condens. Matter* **24**, 273202 (2012).
79. R. G. Burns. Mineralogical Applications of Crystal Field Theory. London and New York (Cambridge University Press) (1970).
80. A. M. Balbashov, A. G. Berezin, Yu. V. Bobryshev, P. Yu. Marchukov, I. V. Nikolaev, Ya. Paches, L. Pust, E. G. Rudashevskii, and V. V. Shushpanov, Orthogonal magnetic "impurity" (Fe^{+3} in c positions) in orthoferrite $YFeO_3$, Zh. Eksp. Teor. Fiz. **102,** 1397 (1992) (Sov. Phys. JETP **75,** 757 (1992)).
81. M. Mrad, A. Tarhini, V. Giordano, Absorbance and energy levels for a Fe^{3+} ion in α-Al_2O_3. Optical pumping applied to a 31 GHz Maser. Eur. Phys. J. Appl Phys **20**, 31001 (2020).
82. M. Mrad, P.-Y. Bourgeois, M. E. Tobar, Y. Kersalé, V. Giordano. Analysis of the whispering gallery mode sapphire Fe^{3+} maser under magnetic field. European Physical Journal: Applied Physics, EDP Sciences, 2012, 57 (2), pp.21005.
83. L. S. Kornienko and A. M. Prokhorov Electronic Paramagnetic Resonance of the Fe^{3+} Ion in Corundum**,** ZhETF **40**, 1594 (1961)- JETP,**13** 1120 (1961).
84. H. F. Symmons and G. S. Bogle, On the Exactness of the Spin-Hamiltonian Description of Fe^{3+} in Sapphire Proc. Phys. Soc.**79**, 468 (1962).
85. M. Mrad, P.Y. Bourgeois, Y. Kersalé, and V. Giordano, Fe^{3+} paramagnetic ion in a-Al_2O_3 energy levels revisited. Application to a 31 GHz Maser proposal arXiv:1201.1760v1 (2012).
86. M. G. Zhao and M. Chiu, Analytical expressions for zero-field splittings of 31 ions in low-symmetry fields and their applications, Phys. Rev. B **52**, 10043 (1995).
87. S. Lyubutin, T. V. Dmitrieva, and A. S. Stepin., Dependence of exchange interactions on chemical bond angle in a structural series:cubic perovskite–rhombic orthoferrite–

rhombohedral hematite (Zh. Eksp. Teor. Fiz. **115**, 1070 (1999)), J. Exp. Theor. Phys. **88**, 590 (1999).

88. B. Bleaney and R. S. Trenam Paramagnetic resonance spectra of some ferric alums, and the nuclear magnetic moment of ^{57}Fe Proc. Roy. Soc. A **223**, 15 (1954)
89. M. G. Zhao and M. Chiu Substitution site of the Fe^{3+} impurity in crystalline $LiNbO_3$ Phys. Rev. B **49**, 12556 (1994).
90. https://chem.libretexts.org/Bookshelves/Physical_and_Theoretical_Chemistry_Textbook_Maps/Supplemental_Modules_(Physical_and_Theoretical_Chemistry)/Spectroscopy/Magnetic_Resonance_Spectroscopies/Electron_Paramagnetic_Resonance/EPR_-_Theory
91. E. Magome, C. Moriyoshi, Y. Kuroiwa, A. Masuno, and H. Inoue, Noncentrosymmetric Structure of $LuFeO_3$ in Metastable State, Jpn. J. Appl. Phys. **49** 09ME06 (2010).
92. X. Xu and W. Wang, Multiferroic hexagonal ferrites (h-$RFeO_3$, R = Y, Dy-Lu): a brief experimental review, Mod. Phys. Lett. B **28**, 1430008 (2014).
93. A. K. Choquette, C. R. Smith, R. J. Sichel-Tissot, E. J. Moon, M. D. Scafetta, E. Di Gennaro, F. Miletto Granozio, E. Karapetrova, and S. J. May, Octahedral rotation patterns in strained $EuFeO_3$ and other *Pbnm* perovskite films: Implications for hybrid improper ferroelectricity, Phys. Rev. B **94**, 024105 (2016).
94. E. Bousquet and A. Cano Non-collinear magnetism in multiferroic perovskites J. Phys.: Condens. Matter **28** 123001 (2016).
95. L. T. Tsymbal, Y. B. Bazaliy, V. N. Derkachenko, V. I. Kamenev, G. N. Kakazei, F. J. Palomares, and P. E. Wigen, Magnetic and structural properties of spin reorientation transitions in orthoferrites. J. Appl. Phys. **101**, 123919 (2007).
96. Y. B. Bazaliy, L. T. Tsymbal, G. N. Kakazei and P. E. Wigen, The role of erbium magnetization anisotropy during the magnetic reorientation transition in $ErFeO_3$,J. of Appl. Phys. **95**, 6622 (2004).
97. H. Pinto, G. Shachar, H. Shaked, and S. Shtrikman Spin Reorientation in $ErFeO_3$ Single Crystals Observed by Neutron Diffraction Phys. Rev. B **3**, 3861 (1971).
98. G. Gorodetsky, L. M. Levinson, S. Shtrikman, D. Treves, and B. M. Wanklyn, Direct Observation of Spin Rotation in $ErFeO_3$ Phys. Rev. **187**, 637 (1969)

99. R.W.Grant and S.Geller Mechanism of spin reorientation in $ErFeO_3$ Sol. St. Commun. **7** 1291 (1969).

100. R. C. LeCraw, R. Wolf, E. M. Gyorgy, F. B.Hagedorn, J. C. Hensel, and J. P. Remeika, Microwave Absorption near the Reorientation Temperature in The Rare Earth Orthoferrites, J. Appl. Phys. **39**, 1019 (1968).

101. R. P. Chaudhury, B. Lorenz, C. W. Chu, Ya. B. Bazaliy and L. T. Tsymbal, Lattice strain and heat capacity anomalies at the spin reorientation transitions of ErFeO3 orthoferrite, *J. Phys.: Conf. Ser.* **150,** 042014 (2009).

102. G. Gorodetsky, R. M. Hornreich, I. Yaeger, H. Pinto, G. Shachar, and H. Shaked. Magnetic structure of $ErFeO_3$ below 4.5 K. Phys. Rev. B **8**, 3398 (1973).

103. I. Fita, R. Puzniak, E. E. Zubov, P. Iwanowski, and A. Wisniewski Temperature-driven spin switching and exchange bias in the ErFeO3 ferrimagnet Phys. Rev. B **105**, 094424 (2022).

104. V.N. Derkachenko, A.M. Kadomtseva, V.A. Timofeeva, and V.A. Khokhlov Temperature hysteresis of the magnetization in orthoferrites at the compensation point JETP Lett **200**, 236 (1974).

105. R. V. Mikhaylovskiy, E. Hendry, V. V. Kruglyak, R. V. Pisarev, Th. Rasing, and A. V. Kimel Terahertz emission spectroscopy of laser-induced spin dynamics in TmFeO3 and ErFeO3 orthoferrites in $ErFeO_3$. Phys. Rev. **90**, 184405 (2014).

106. R. V. Mikhaylovskiy, T. J. Huisman, V. A. Gavrichkov, S. I. Polukeev, S. G. Ovchinnikov, D. Afanasiev, R. V. Pisarev, Th. Rasing, and A. V. Kimel, Resonant Pumping of d−d Crystal Field Electronic Transitions as a Mechanism of Ultrafast Optical Control of the Exchange Interactions in Iron Oxides Phys. Rev. Lett. 125, 157201 (2020).

107. M. P. Zic, Wesley T. Fuhrman, K. Wang, S. Ran, J. Paglione, and N. P. Butch Coupled spin waves and crystalline electric field levels in candidate multiferroic $ErFeO_3$ J. Appl. Phys. **130**, 014102 (2021).

108. G. Deng, P. Guo, W. Ren, S. Cao, H. E. Maynard-Casely,M. Avdeev, and G. J. McIntyre, The magnetic structures and transitions of a potential multiferroic orthoferrite $ErFeO_3$ J. of Appl. Phys. **117**, 164105 (2015).

109. M. P. Zic, Wesley T. Fuhrman, K. Wang, S. Ran, J. Paglione, and N. P. Butch Coupled spin waves and crystalline electric field levels in candidate multiferroic $ErFeO_3$ J. Appl. Phys. **130**, 014102 (2021).
110. D. L. Wood, L. M. Holmes, and J. P. Remeika, Exchange Fields and Optical Zeeman Effect in $ErFeO_3$Phys. Rev. **185**, 689 (1969).
111. M. E. Lines and A. M. Glass, Principles and Applications of Ferroelectrics and Related Material (Oxford University Press, Oxford) 2001.

Figure Captions

Figure 1. (color online) Change of rare earth coordination number in the orthorhombic perovskite polyhedral A site as the lanthanide ionic radius decreases from La^{3+} to Lu^{3+} distorting the higher temperature cubic phase AO_{12} cage [11, 41, 42, 44, 45].

Figure 2. (color online) (a) Zone center temperature antiferromagnetic (ω_{AFM}) and ferromagnetic (ω_{FM}) magnon modes of $LaFeO_3$ using the 110 K spectrum as normalizing reference; (b) Zone center temperature dependent first excited state of the $Pr^{3+(}4f^{2})$ $^3H_4$ manifold and weaker side bands assigned to the ω_{AFM} and ω_{FM} resonances in $PrFeO_3$ using the 110 K spectrum as normalizing reference. Inset; details showing the undergoing peak softening in the 5 K to ~2.0 K interval**. (**c) Zone center temperature dependence of the band associated to defect site Fe^{3+} and antiferromagnetic (ω_{AFM}) and ferromagnetic (ω_{FM}) magnon modes of $LuFeO_3$ using the 110 K spectrum as normalizing reference.

Figure 3. (color online) $LaFeO_3$ antiferromagnetic and ferromagnetic spin wave resonances as function of the applied magnetic field B_0 at 5 K. Inset: peak positions of the shown absorptions after gaussian fits (Fig. S5).

Figure 4. (color online) First excited state of the $Pr^{3+(}4f^{2})$ $^3H_4$ manifold and weaker side bands assigned to the ω_{FM} and ω_{AFM} resonances in $PrFeO_3$ as function of the applied magnetic field B_0 at 5 K. Inset: Inset: peak positions of the shown absorptions after gaussian and Weibull fits (Fig. S8).

Figure 5. Zone center Fe^{3+} **(**$^6A_1$) crystal field transition and antiferromagnetic ω_{AFM} and ferromagnetic ω_{FM} magnon modes of $LuFeO_3$ as function of the applied magnetic field B_0 at 5 K. Inset: peak positions of the shown absorptions after gaussian and Weibull fits. (Fig. S10).

Figure 6. (color online) $ErFeO_3$ sequential absorption ratios $(B_{0j}+0.5T)/B_{0j}$, B_{0j} is the applied field at the jth incremental step, projecting field dependent Zeeman splits of Fe^{3+} ($^6A_1$) and Er^{3+} ($^4I_{15/2}$) and resonant magnon mode (dashed arrows) at the compensation temperature ~ 40 K. Note that both resonances are inside a triangle defined by the highest Fe^{3+} ($^6A_1$) and the lowest Er^{3+} ($^4I_{15/2}$)

branch exchange converging at ~5 T. The olid arrow points to the anomaly associated to paramagnetic Er^{3+}.

Figure 7. (color online) (a) $ErFeO_3$ temperature dependent of the resonance ratios using the 108 K spectrum as reference, inset: same data vertically displaced showing the convergence of both rmagnons toward the onset of the lower temperature Γ_1 representation;(b) Applied field dependent $ErFeO_3$ magnon absorption in the ZFC Γ_1 (A_x, G_y, C_z) phase, at 2.4 K, below and at the interfering Fe^{3+} Zeeman field split.

Figure 8. (color online) $ErFeO_3$ absorption ratios (B_{0J}/0.0T), B_{0j} is the applied field at the jth incremental step, for the THz excitations and exchange biased zone center Fe^{3+}($^6A_1$**)** Zeeman split at 5 K. The full line in the back panel shows memory effects brought up by calculating the ratio of spectra of measurements done at the initial and end run at zero field and 5 K.

Figure 9 (color online) (a) applied field dependent Zeeman split of Fe^{3+} ($^6A_1$) and Γ_2 magnons, left axis: sequential absorption ratios (B_{0j}+0.5T)/B_{0j}, B_{0j} is the applied field at the jth incremental step at 5 K, right axis: sequential absorption ratios B_{0j}/(B_{0j}+0.5T) calculated decreasing fields at 5 K.(b) Applied field dependent Zeeman split of Fe^{3+} ($^6A_1$) , left axis: sequential absorption ratios (B_{0j}+0.5T)/B_{0j}, B_{0j} is the applied field at the jth incremental step at 2.4 K, right axis: sequential absorption ratios B_{0j}/(B_{0j}+0.5T) calculated decreasing fields at 2.4 K. The measured profiled for the Γ_1 magnon is shown centered at ~28.5 cm^{-1}.

Figure 10. (color online) $ErFeO_3$ far infrared absorption, reflectivity, and 1.0 T/0.0 T ZFC absorption ratio at 5 K. (a) Dashed lines: $ErFeO_3$ powder embedded polyethylene pellet absorption spectra at 0 T and 1 T; circle and full line: polycrystal reflectivity spectra and multioscillator fit respectively; full lines: 1.0 T/0.0 T ZFC absorption ratio; asterisks: peak position for the 49.5 cm^{-1} (6.14 meV) , 110.5 cm^{-1} (13.7 meV) and 167.3 cm^{-1} (20.74 meV) transitions of the Er^{3+} ($^4I_{15/2}$) manifold; (b) vertically displaced reflectivity of $RFeO_3$. (R=La, triangle; Er, square; Lu, diamond) showing relative changes in the R^{3+}-O vibrational profiles induced by the change in the lanthanide size at 80 K. Asterisks: ZCF transitions of the Er^{3+} ($^4I_{15/2}$) manifold associated to lattice phonons at the respective frequencies.

Figure 11. (color online) (a) $ErFeO_3$ powder embedded polyethylene pellet absorption spectra at 0 T and 1 T peaking at the 49.5 cm^{-1} (6.14 meV), 110.5 cm^{-1} (13.7 meV), and 167.3 cm^{-1} (20.74 meV) transitions of the Er^{3+} ($^4I_{15/2}$) manifold; (b), (c), (d) vertically offset Zeeman split sequential absorption ratios $(B_{0j}+0.5T)/B_{0j}$, B_{0j} is the applied field at the jth incremental step, of the Er^{3+} ($^4I_{15/2}$) levels showing the bias induced by the Fe^{3+} exchange on the lower frequency branch (see also Fig.S17).

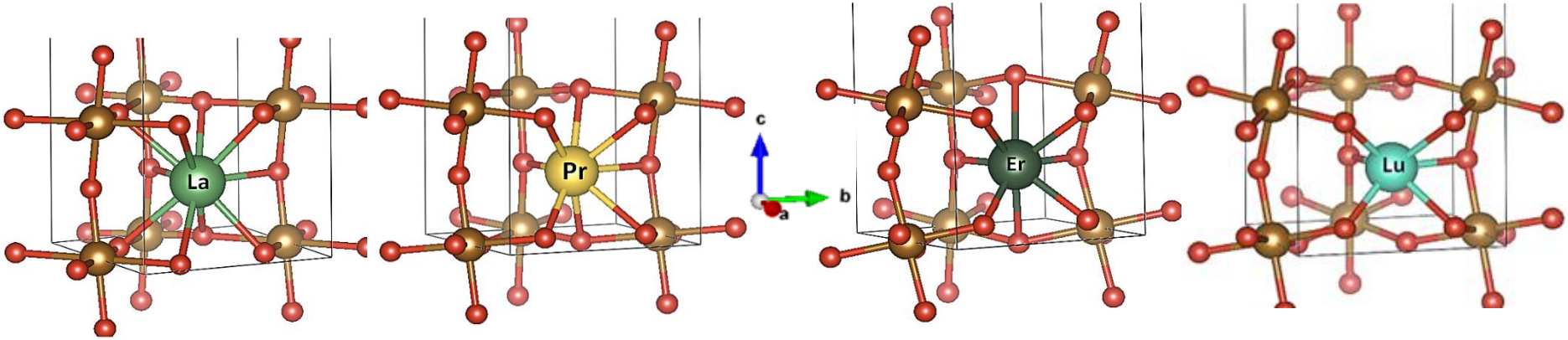

Coordination number 10 **Coordination number 8** **Coordination number 8** **Coordination number 6**

Fig. 1
MASSA et al

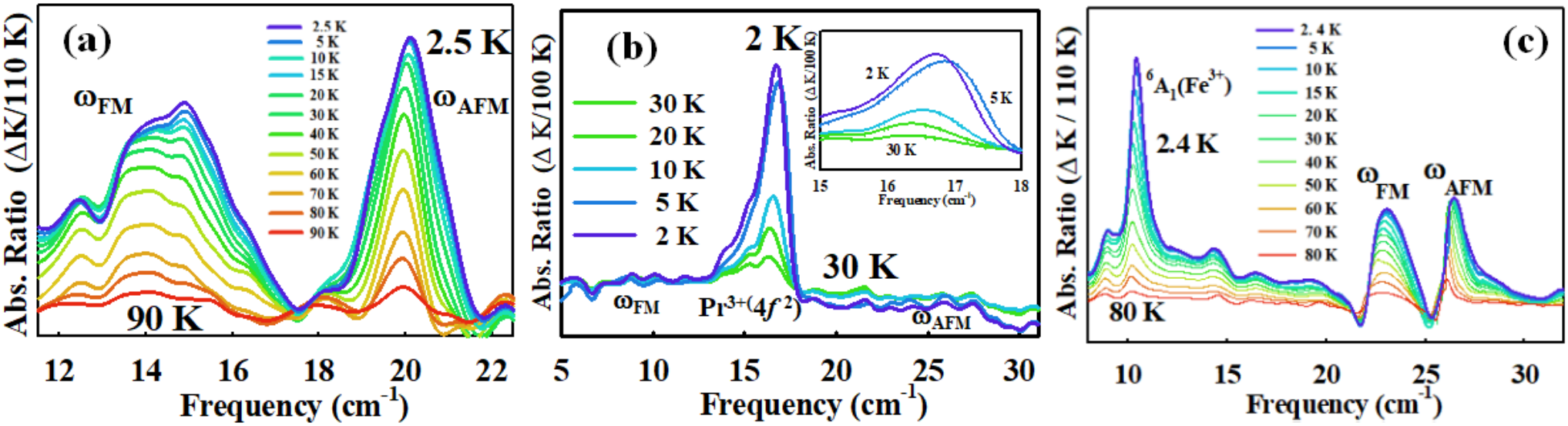

Fig. 2
MASSA et al

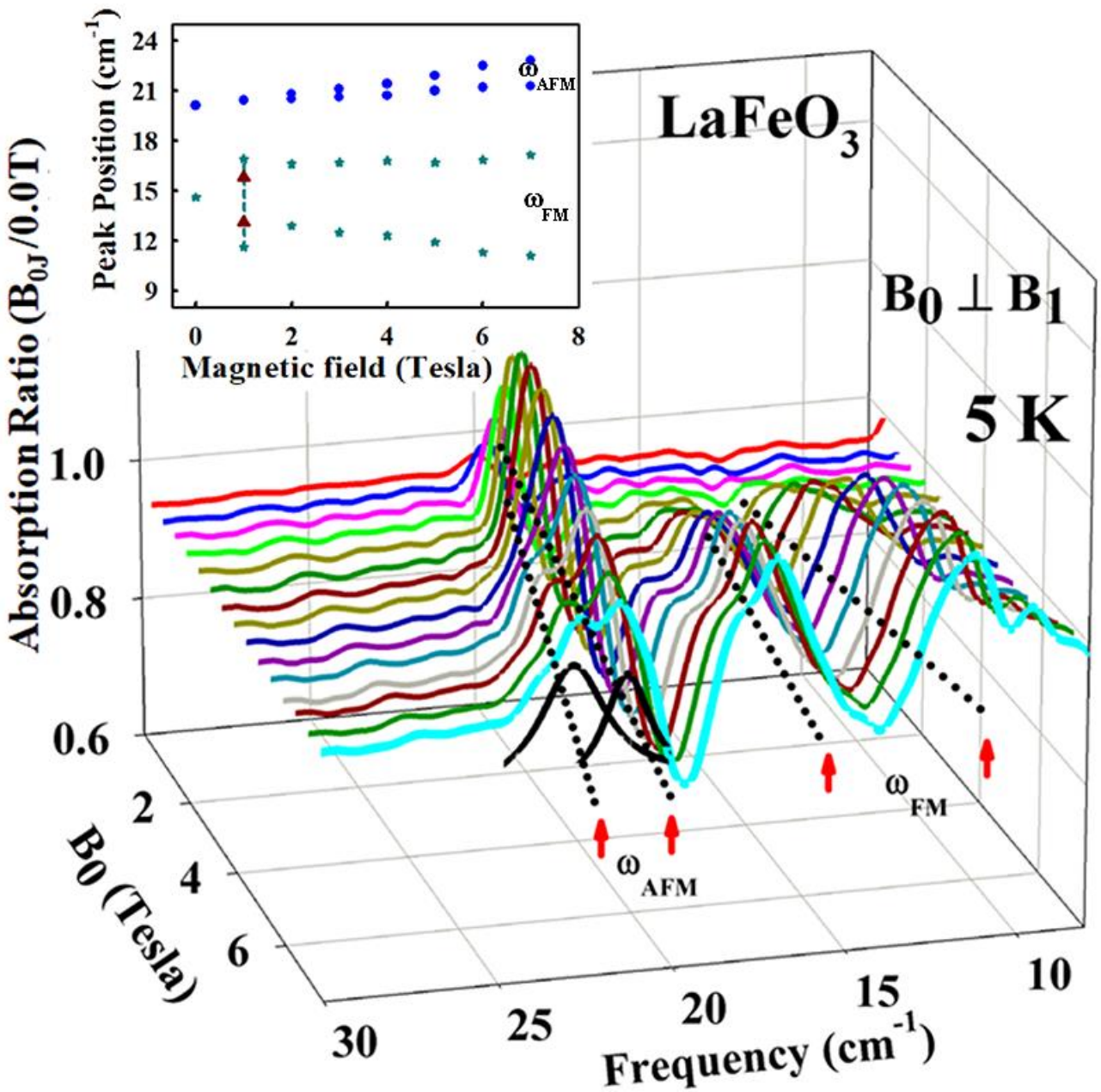

Fig. 3
MASSA et al

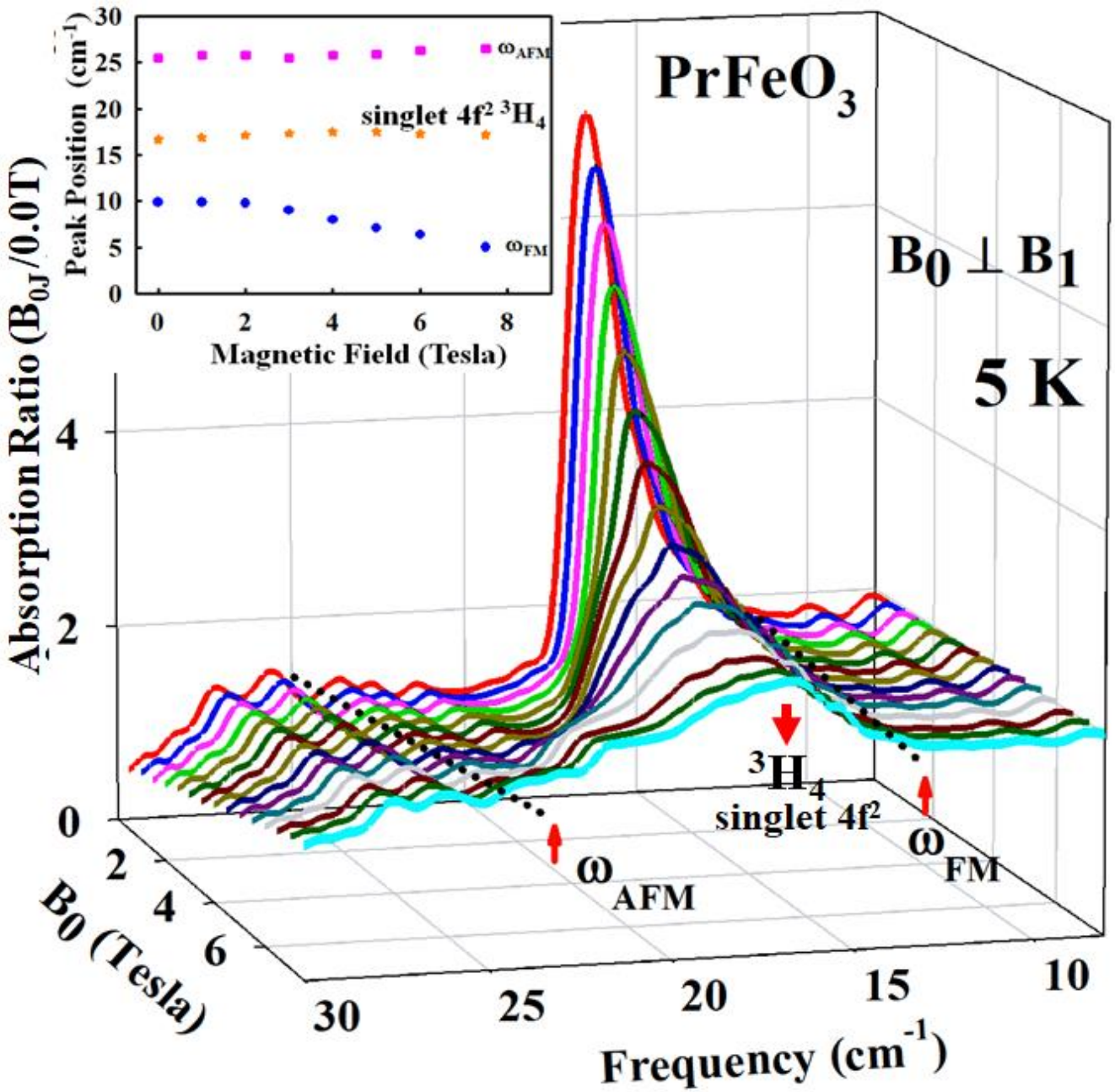

Fig. 4
MASSA et al

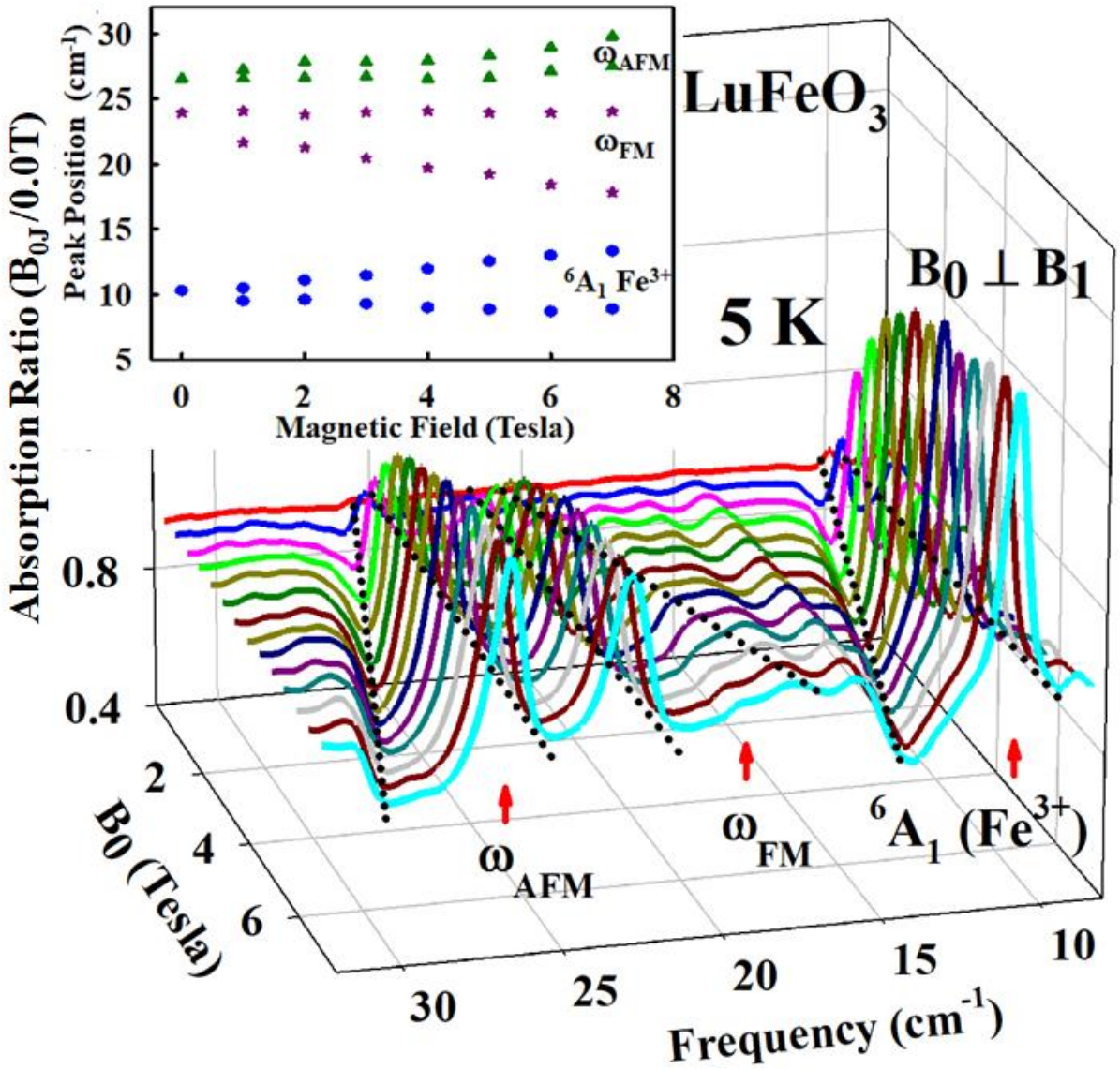

Fig. 5
MASSA et al

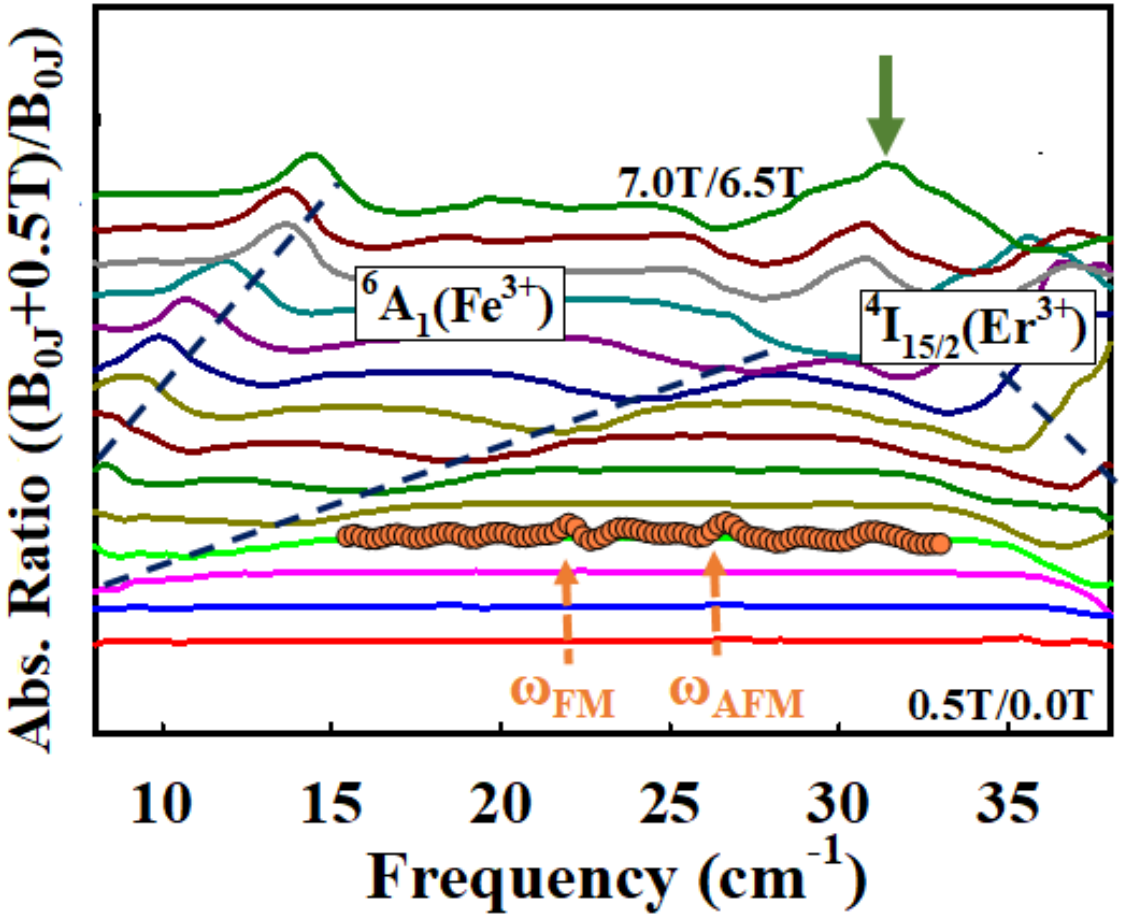

Fig. 6
MASSA et al

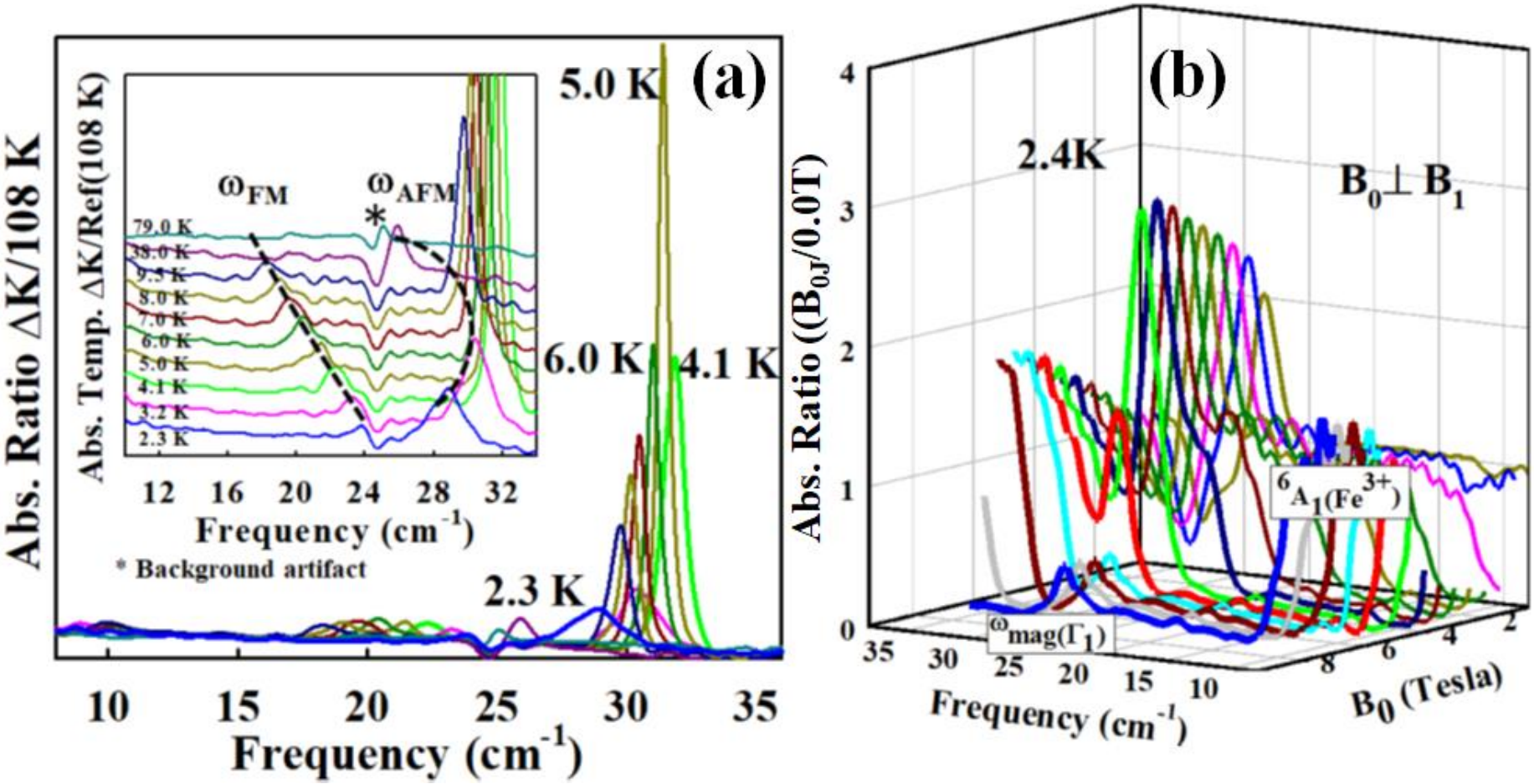

Fig. 7
MASSA et al

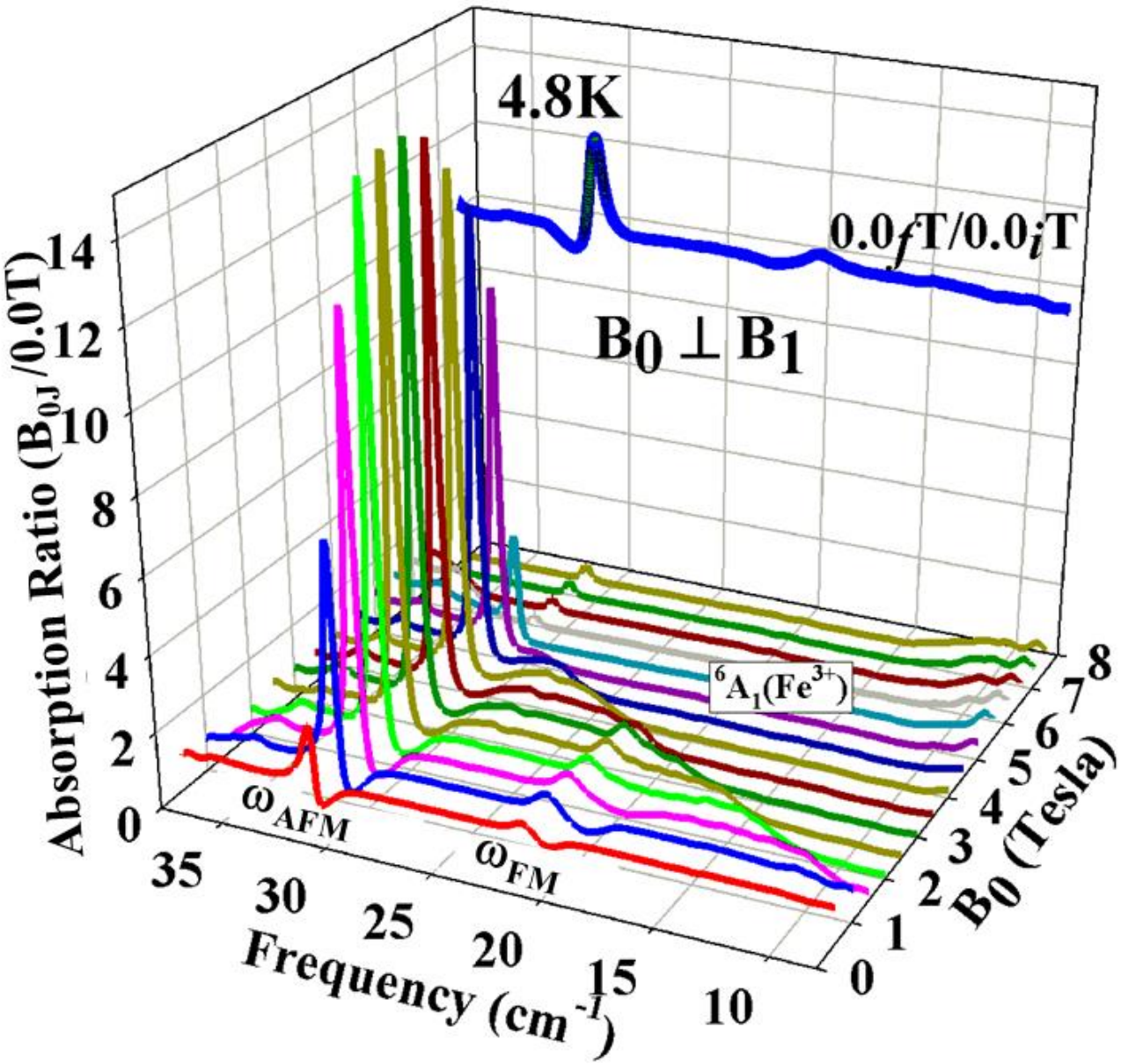

Fig. 8
MASSA et al

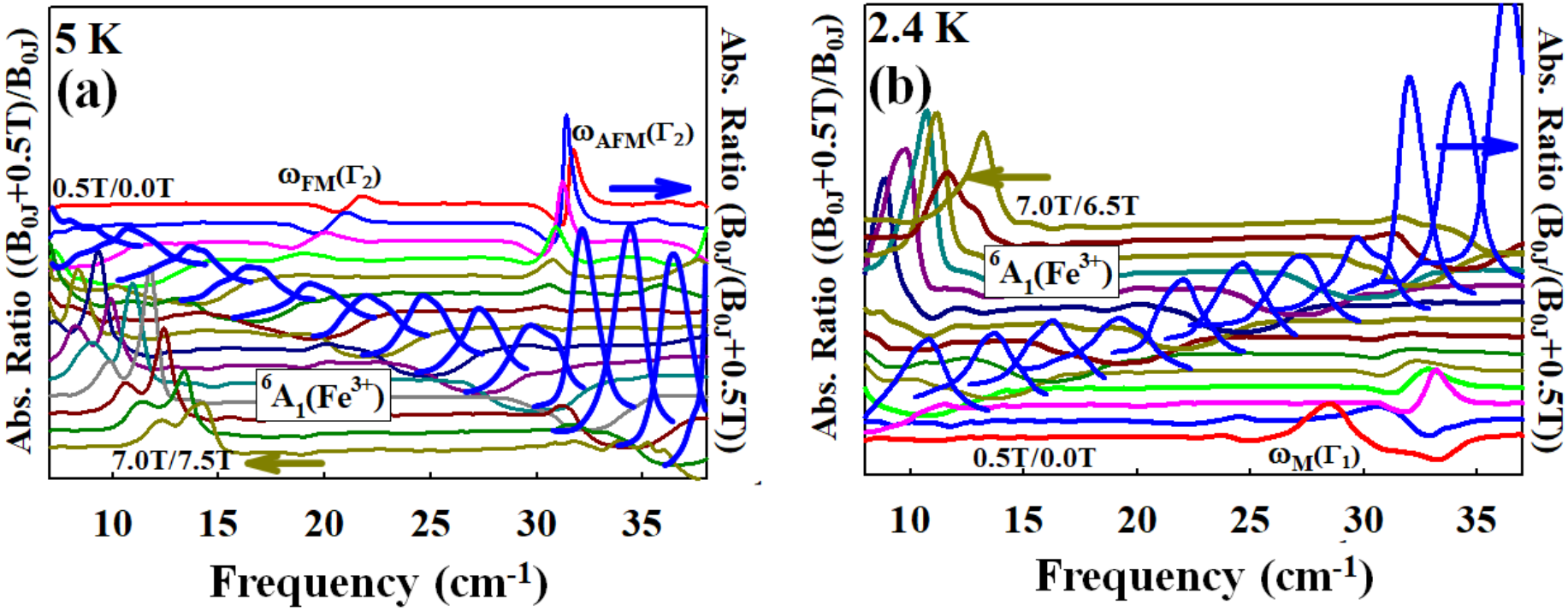

Fig. 9
MASSA et al

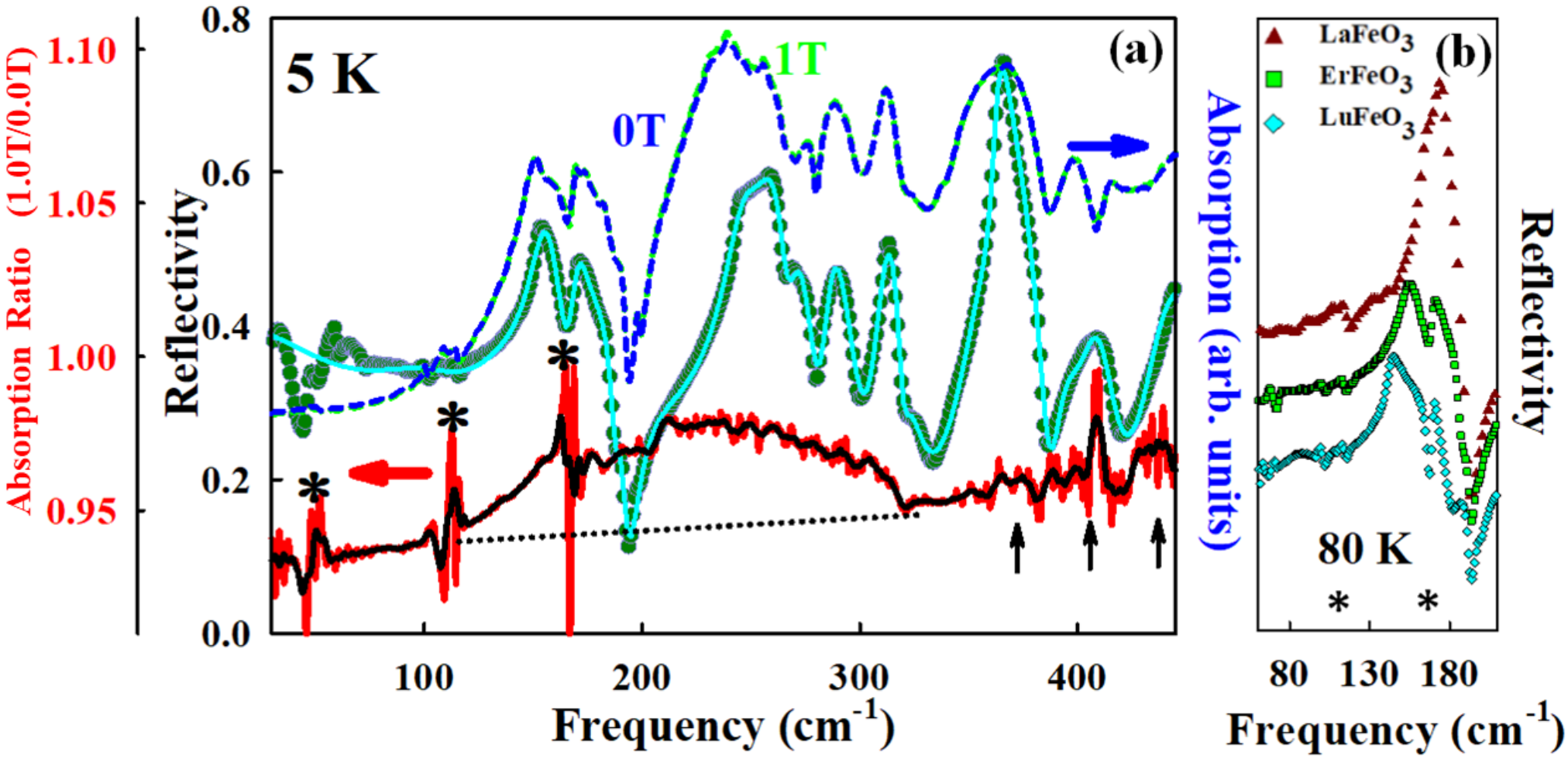

Fig. 10
MASSA et al

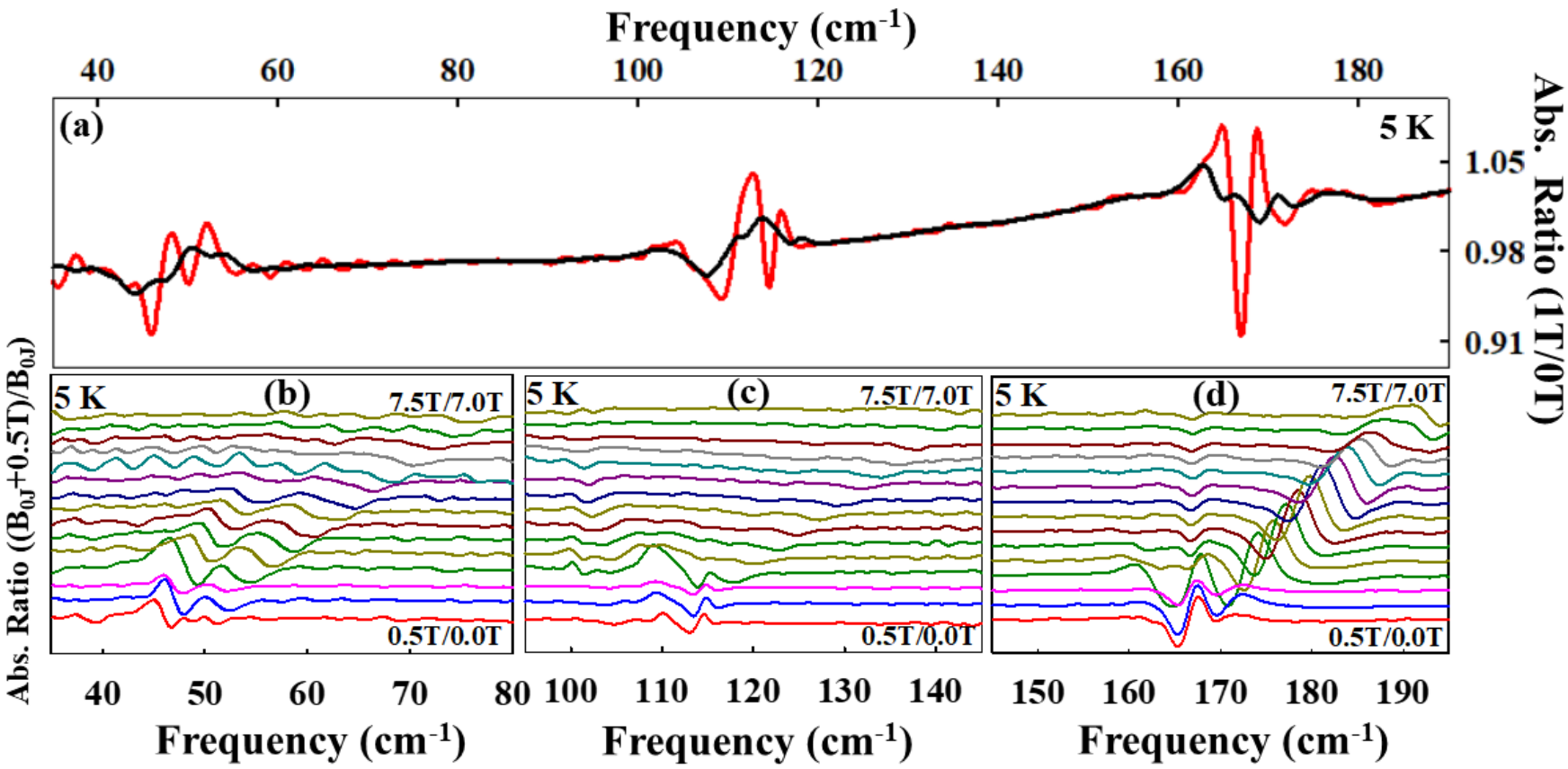

Fig. 11
MASSA et al

SUPPLEMENTAL MATERIAL

Low Temperature Terahertz Spectroscopy of $LaFeO_3$, $PrFeO_3$, $ErFeO_3$, and $LuFeO_3$: magnon resonances and ground multiplet transitions

Néstor E. Massa,*[,1] Leire del Campo,[2] Vinh Ta Phuoc,[3] Paula Kayser,[4‡] and José Antonio Alonso[5]

[1] Centro CEQUINOR, Consejo Nacional de Investigaciones Científicas y Técnicas, Universidad Nacional de La Plata, Bv. 120 1465, B1904 La Plata, Argentina.

[2] Centre National de la Recherche Scientifique, CEMHTI UPR3079, Université Orléans, F-45071 Orléans, France.

[3]Groupement de Recherche Matériaux Microélectronique Acoustique Nanotechnologies-Université François Rabelais Tours, Faculté des Sciences & Techniques, F- 37200 Tours, France.

[4]Centre for Science at Extreme Conditions and School of Chemistry, University of Edinburgh, Kings Buildings, Mayfield Road, EH9 3FD Edinburgh, United Kingdom.

[5]Instituto de Ciencia de Materiales de Madrid, CSIC, Cantoblanco, E-28049 Madrid, Spain.

‡ Present address: Departamento de Química Inorgánica, Facultad de Ciencias Químicas, Universidad Complutense de Madrid, 28040 Madrid, Spain.

Corresponding author:
Néstor E. Massa *e-mail: neemmassa@gmail.com

SAMPLE PREPARATION, MAGNETIC, and STRUCTURAL CHARACTERIZATION

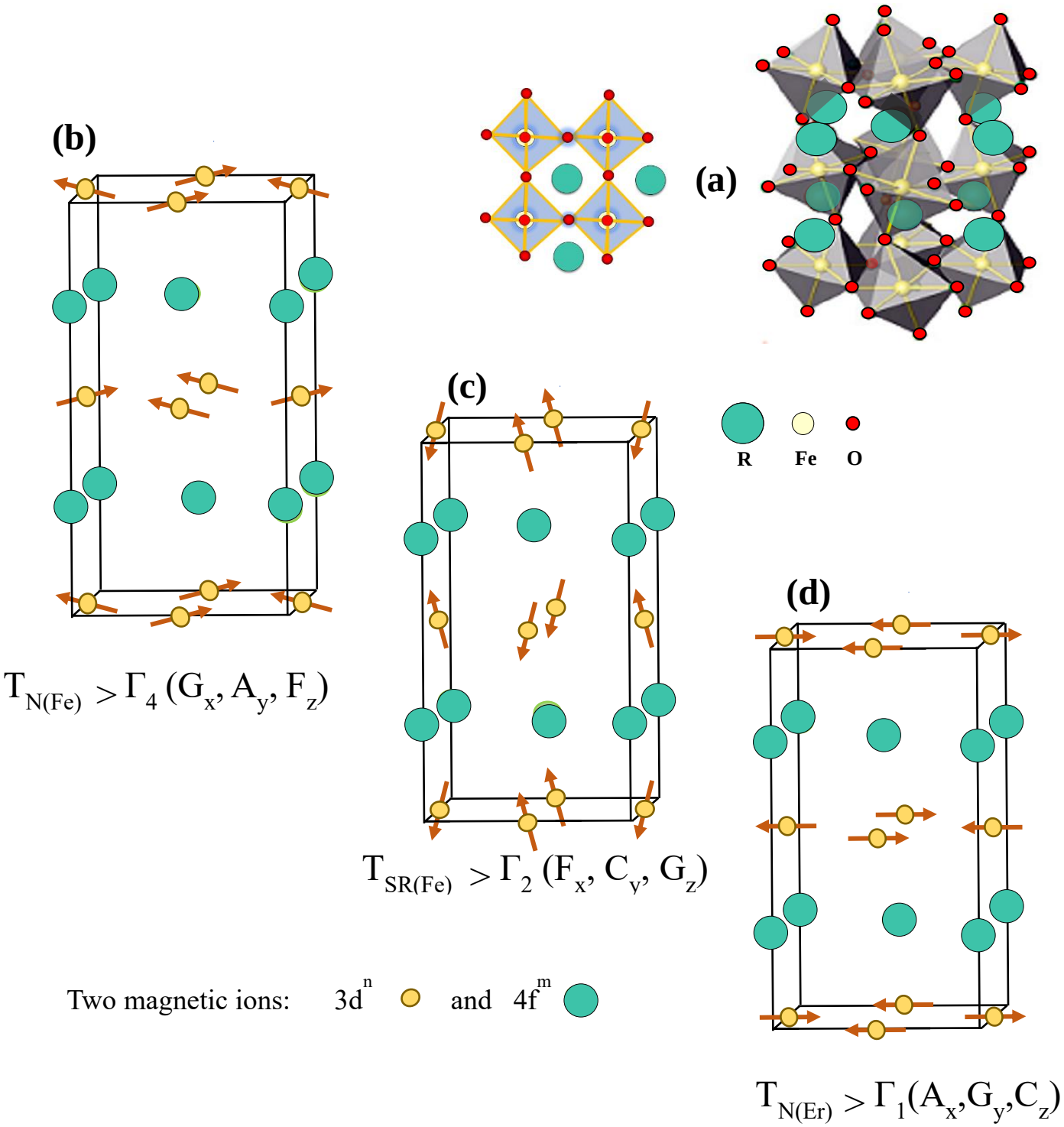

Fig. S1. (a) View of the $RFeO_3$ (R=rare earth) ideal cubic P_{m3m} perovskite and P_{bnm} (D_{2h}^{16}) four molecules per unit cell orthorhombic distorted structure. Fe^{3+} spin structure in the (b) Γ_4 (G_x, A_y, F_z) , (c) Γ_2 (F_x, C_y, G_z), and (d) Γ_1 (A_x, G_y, C_z) representations.

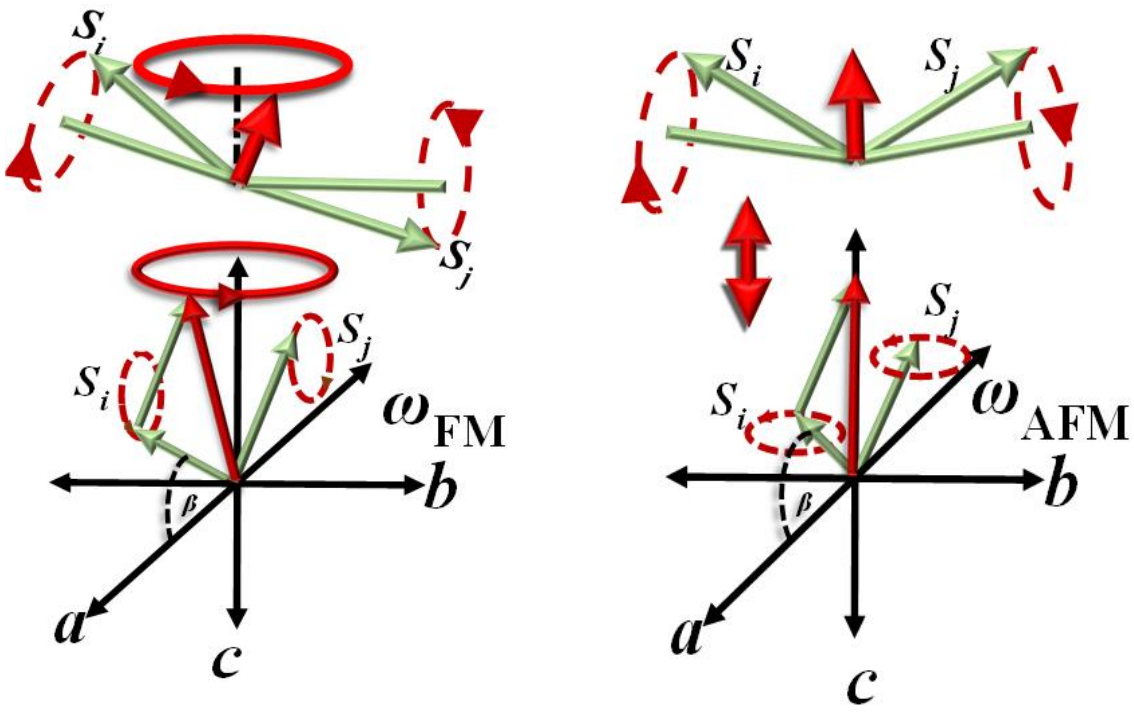

Fig. S2. THz magnetic resonances of optically active spin wave modes in the Γ_4 (G_x, A_y, F_z) representation of orthorhombic distorted perovskites in the P_{bnm} space group. S_i and S_j are the transition metal spins along the ***a*** axis. The ω_{FM} mode receives its name due to distorted low frequency cone defined by the ferromagnetic moment precessing the ***z*** axis. and the ω_{AFM} is built on x,y out-of-phase oscillations and in-phase oscillations along the ***z*** axis (After https://doi.org/10.1016/j.jmmm.2018.07.028 and references therein).

$RFeO_3$ (R= La, Pr, Er, Lu) polycrystalline samples were prepared by standard ceramic synthesis procedures. Stoichiometric amounts of analytical grade Fe_2O_3 and R_2O_3 powder oxides were thoroughly ground and heated in air at 1000ºC for 12 h and 1300ºC for 12 h in alumina crucibles. Then, pellets of ~1cm diameter, less than 2mm thick, were prepared by uniaxial pressing the raw powders and sintering the disks at 1300ºC for 2 h. The purity of the samples for all four $RFeO_3$ (R= La, Pr, Er, Lu) was checked by X-ray powder diffraction (XRD) collected at room temperature with Cu-Kα radiation. Shown in Fig. S3, all data were analyzed using the Rietveld method with refinements carried out with the program FULLPROF.

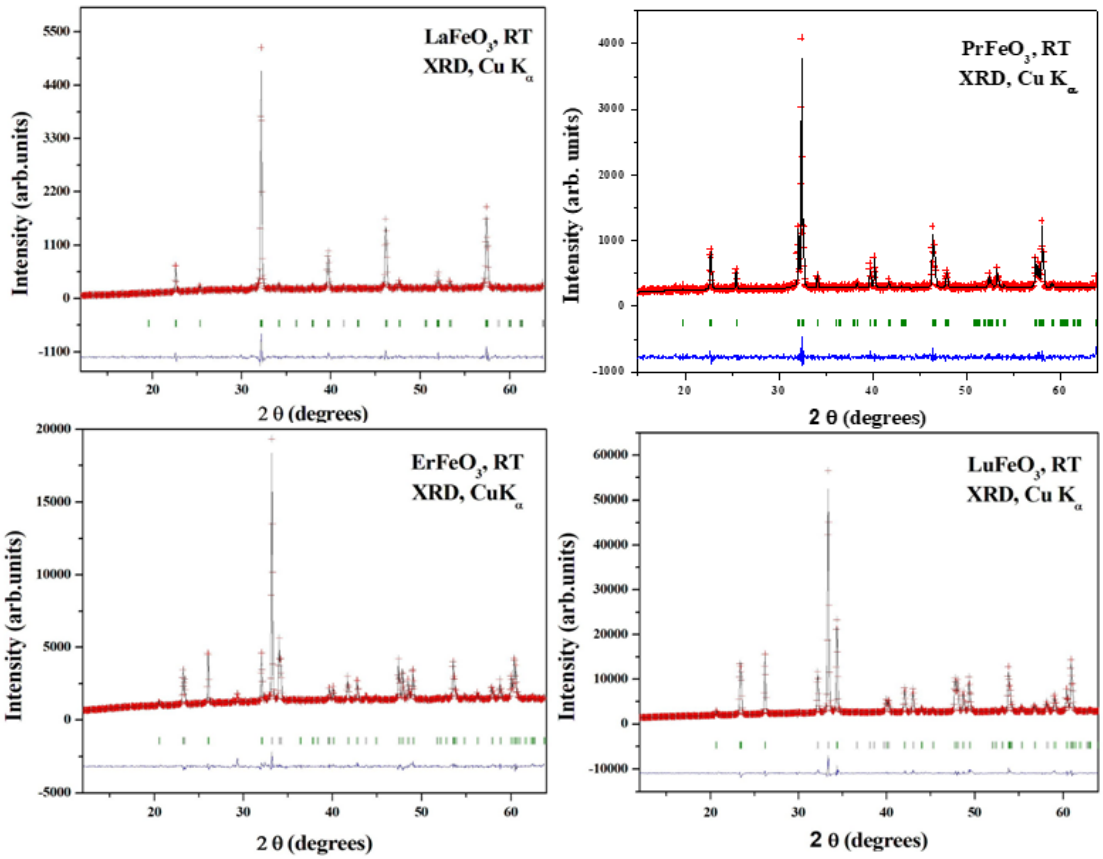

Fig. S3. Fitted X-ray (CuKα) diffraction patterns of $LaFeO_3$, $PrFeO_3$, $ErFeO_3$, and $LuFeO_3$ in the room temperature crystalline space group P_{bmn} (D_{2h}^{16}) with four molecule per unit cell (Z=4). Vertical bars are reflection positions of the orthorhombic unit cell used in the Rietveld refinement. The bottom curve is the difference between the experimental and calculated patterns.

EXPERIMENTAL METHODS AND DATA ANALYSIS

a) THz measurements

Low temperature-low frequency absorption measurements from 3 cm^{-1} to 50 cm^{-1} with 0.5 resolution have been performed in the THz beamline in the low-alpha multi bunch hybrid mode of the BESSY II storage ring at the Helmholtz-Zentrum Berlin (HZB) [1] In the synchrotron low-alpha mode electrons are compressed within shorter bunches of only ~2 ps duration allowing far-infrared wave trains up to mW average power to overlap coherently in the THz range below 50 cm^{-1}. [2,3] All measurements have been done in the Voigt configuration.

To avoid possible artifacts introduced in our spectra by the beam operation our measurements are presented as spectrum ratios, as in fig. 2, in which we normalized lower temperature spectra by a higher temperature spectrum aiming to mostly compensate extrinsic anomalies. For the same reason we use absorption incremental sequential ratios on field dependent measurements (Abs. Ratio $((B_{0J}+0.5T)/B_{0J})$, B_{0j} is the applied field at the jth incremental step, 0.5 is the field step increment in Teslas) since by doing this we were able to verify the absence of run glitches (e.g., fig.6) besides checking the compound magnetic response to the field step increments. the compound magnetic response to the field step increment. This, in turn, allows to now calculate with confidence band features that are induced only by the applied field (e.g., fig. 3), here, using the ZFC spectrum as normalizing reference.

Polyethylene pellets embedded with $ErFeO_3$ powder were used in the far infrared measurements done with the beamline interferometer Bruker IFS125 HR.

We used a superconducting magnet (Oxford Spectromag 4000, here up 7.5 T) interfaced with the interferometer Bruker IFS125 HR for the measurements under magnetic fields**.** The temperature was measured with a calibrated Cernox Sensor from LakeShore Cryotronics mounted to the copper block that holds the sample in the Variable Temperature Insert (VTI) of the Spectromag 4000 Magnet. Measurements in the 30 cm^{-1} to 800 cm^{-1} range were also taken using the internal source of the Bruker IFS125 HR. [2]

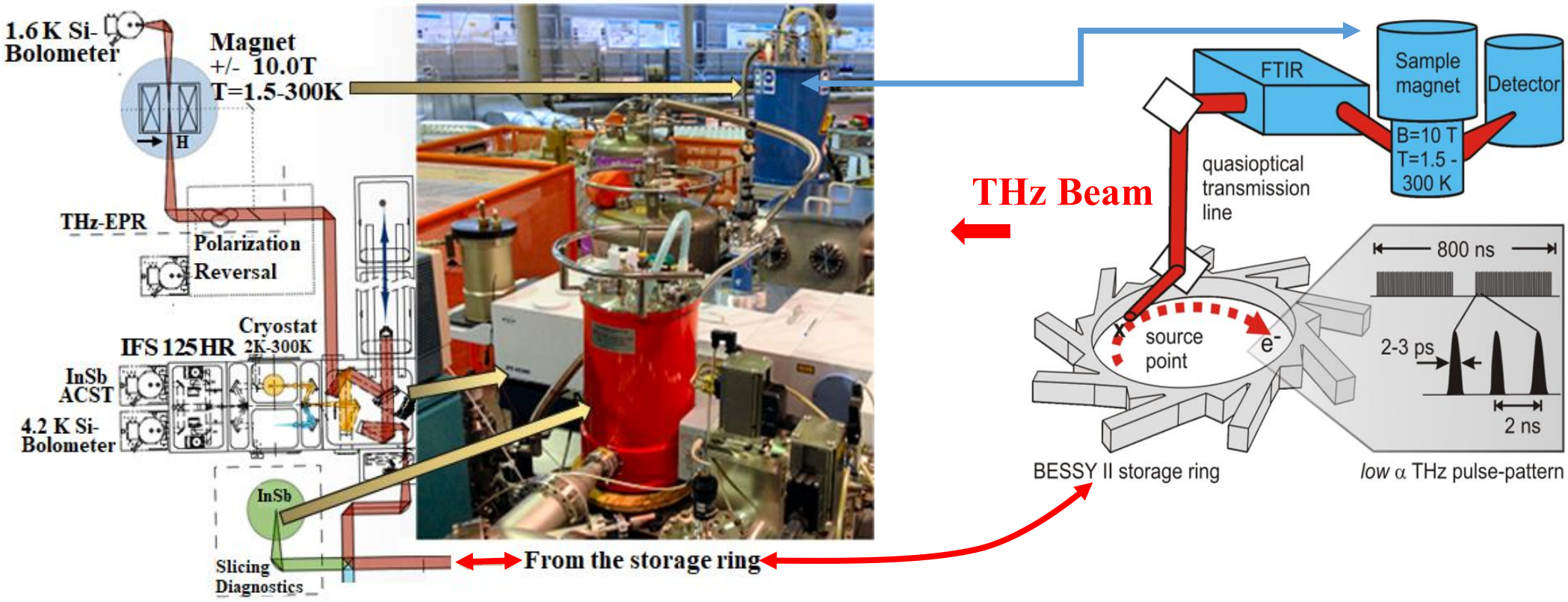

Fig. S4. Beam optical path and layout of the THz beamline at BESSY II [1-3]

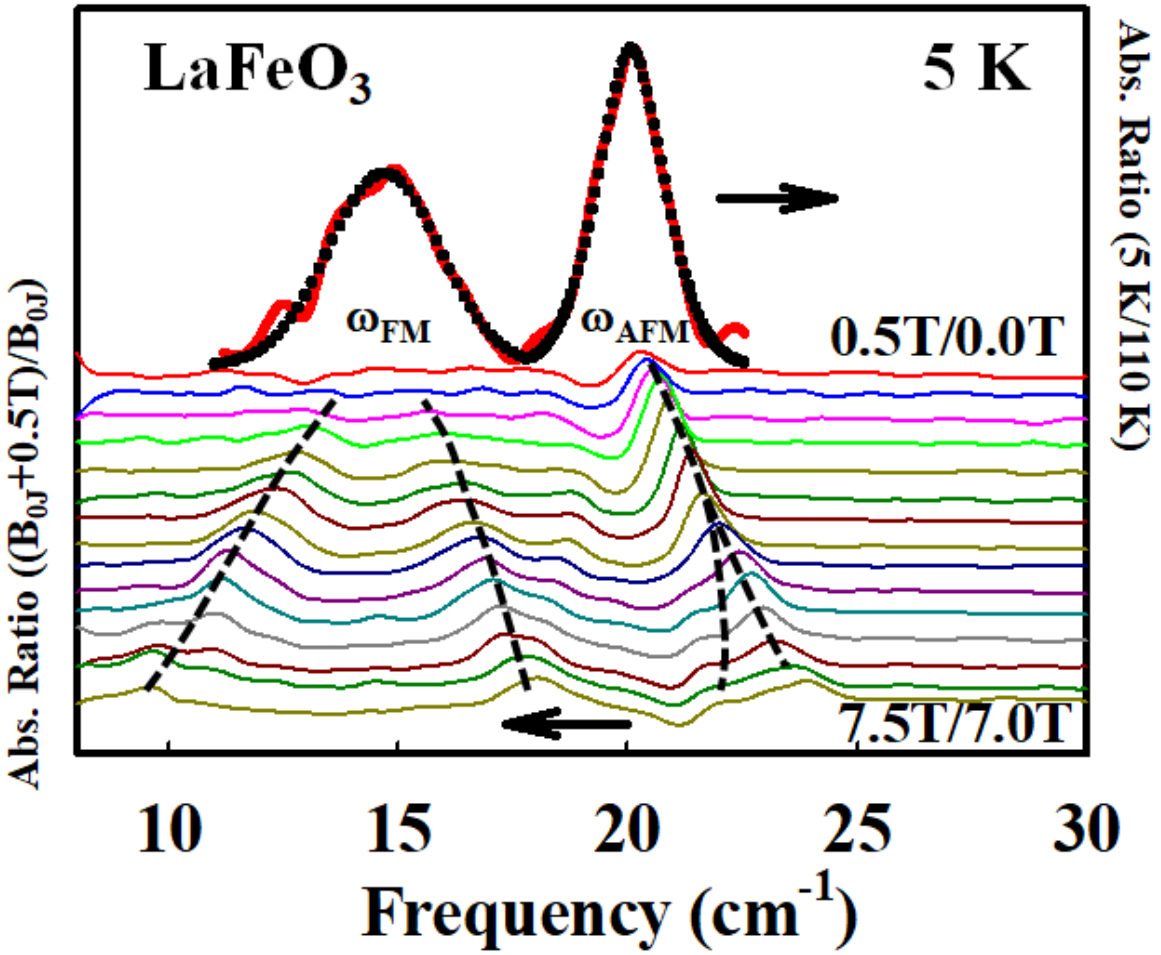

Fig. S5. Upper panel: $LaFeO_3$ 5K zone center antiferromagnetic (ω_{AFM}) and ferromagnetic (ω_{FM}) spin wave resonances; full line: measurement, dots: Gaussian fit. Lower panel: sequential absorption ratios, $(B_{0j}+0.5T)/B_{0j}$, B_{0j} is the applied field at the jth incremental step, 0.5 is the field step increment in Teslas. Dashed lines are guides for the eye.

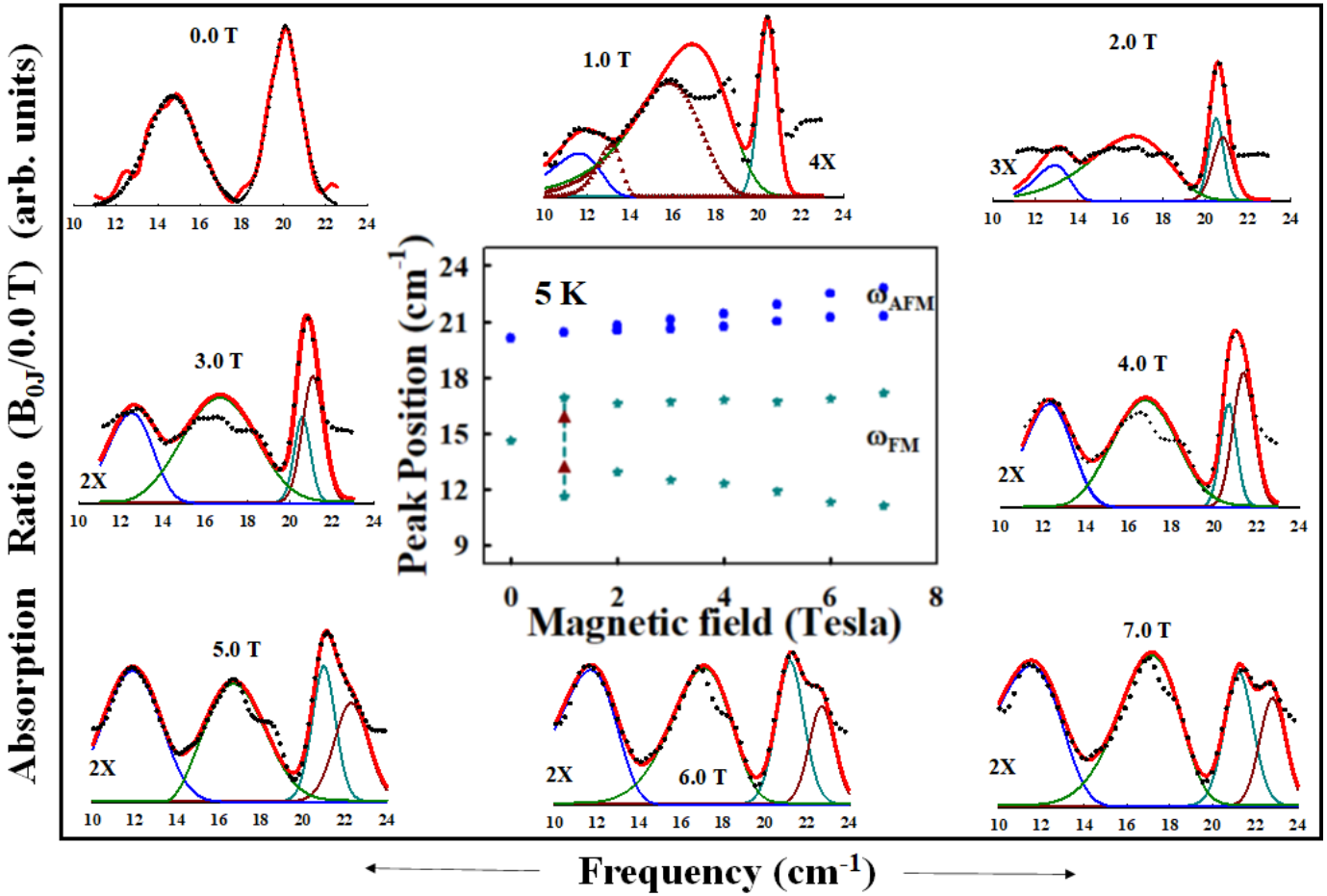

Fig. S6. $LaFeO_3$ antiferromagnetic and ferromagnetic spin wave resonances as function of the applied magnetic fields. Insets: zero field cooled 0.0 T absorption and absolute field induced absorption resonance ratios from 1.0T to 7.0T at 5 K, dots: measurement, full lines: Gaussian and Weibull fits. The bands delineated with upper triangles in the 1.0T inset are the profile main constituents centered at 15.8 cm^{-1} and 13.1 cm^{-1}. Center inset: peak positions of the shown absorptions.

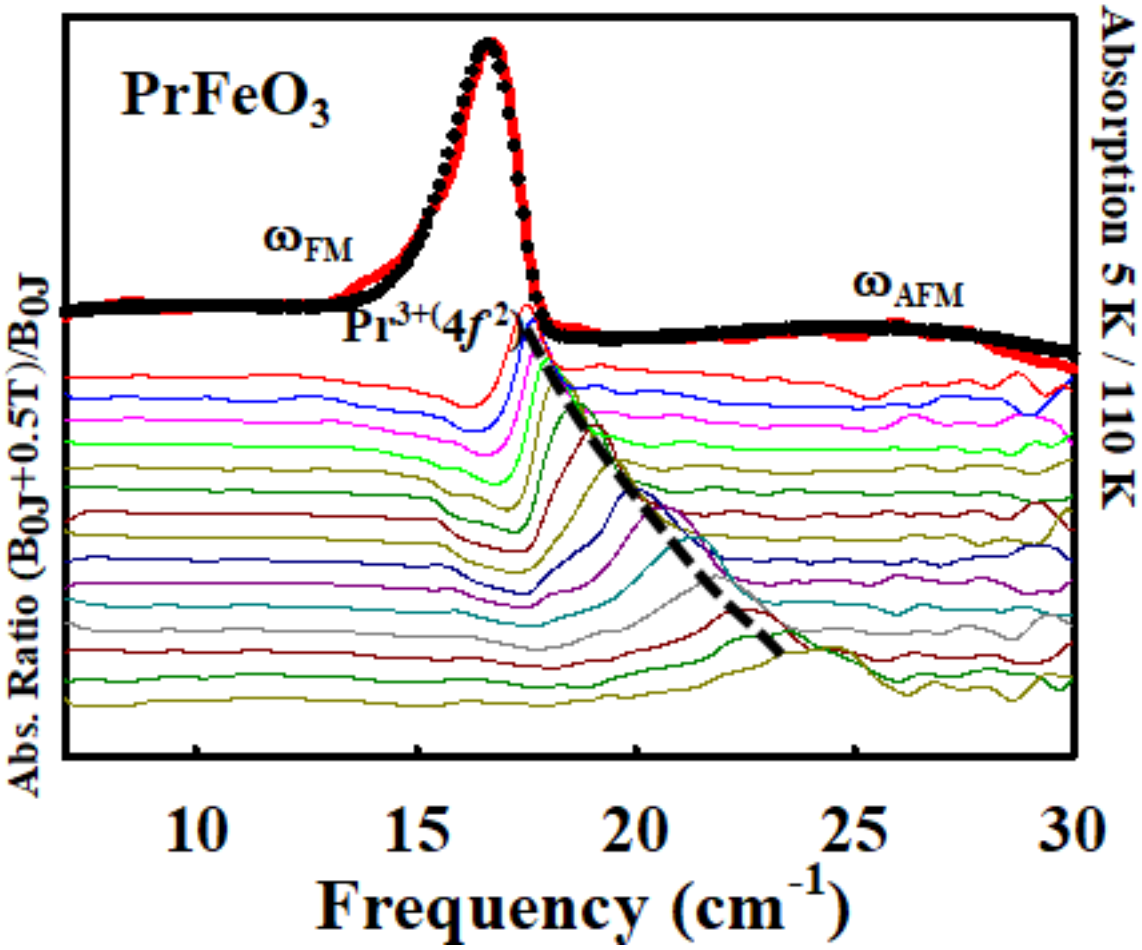

Fig. S7 Upper panel: $Pr^{3+}(4f^2)$ $^3H_4$ ground state singlet and poorly defined bands assigned to ω_{FM} and ω_{AFM} magnon profiles at 5 K in $PrFeO_3$ (see text); full line: measurement, dots: Gaussian and Weibull fits. Lower panel: sequential absorption ratios, $(B_{0j}+0.5T)/B_{0j}$, B_{0j} is the applied field at the jth incremental step, B_{0j} is the applied field at the jth incremental step, 0.5 is the field step increment in Teslas. Dashed line is a guide for the eye.

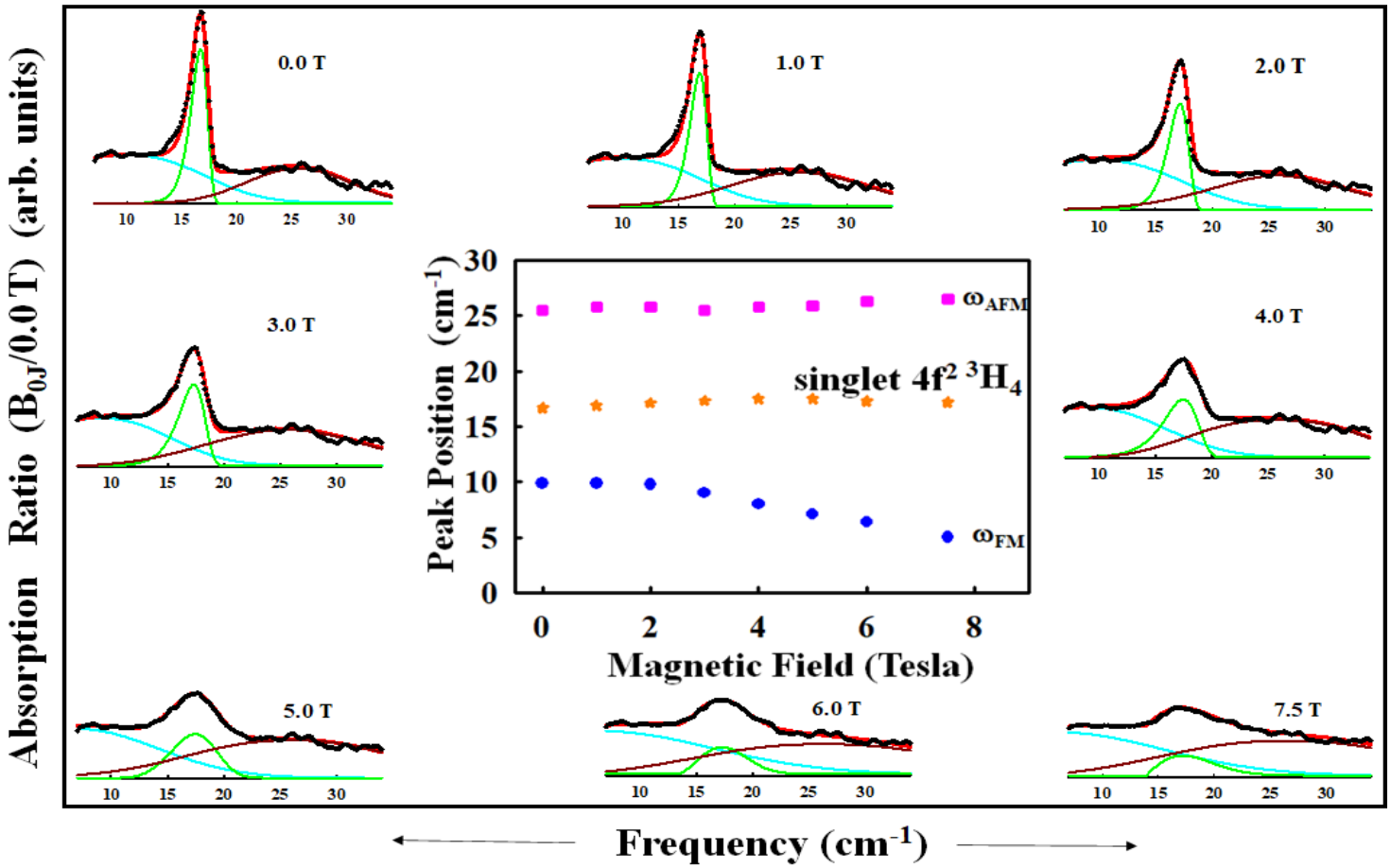

Fig. S8 Singlet lowest crystal field level of the Pr^{3+} ($^3H_4$) manifold at selected magnetic fields and Gaussian deconvolutions of the broader and weaker side bands assigned to the ferromagnetic (ω_{FM}) and antiferromagnetic (ω_{AFM}) resonances at 5 K. Center inset: peak positions of the shown absorptions

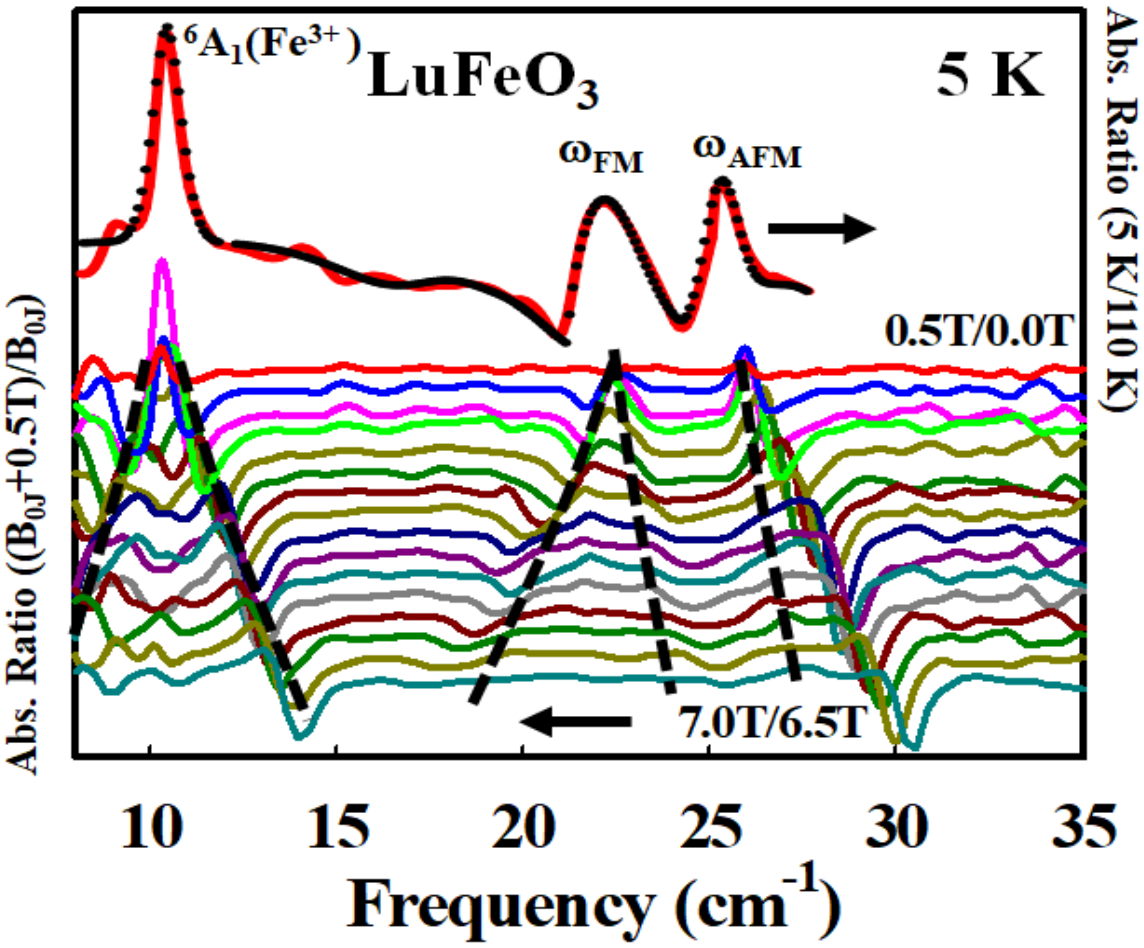

Fig. S9. Upper panel: Zone center Fe^{3+} ($^6A_1$) crystal field transition and antiferromagnetic (ω_{FM}) and ferromagnetic (ω_{AFM}) magnon modes of $LuFeO_3$ at 5 K; full line: measurements, dots: Gaussian fits. Lower panel: sequential absorption ratios, $(B_{0j}+0.5T)/B_{0j}$, B_{0j} is the applied field at the jth incremental ste , 0.5 is the field step increment in Teslas. Dashed lines are guides for the eye.

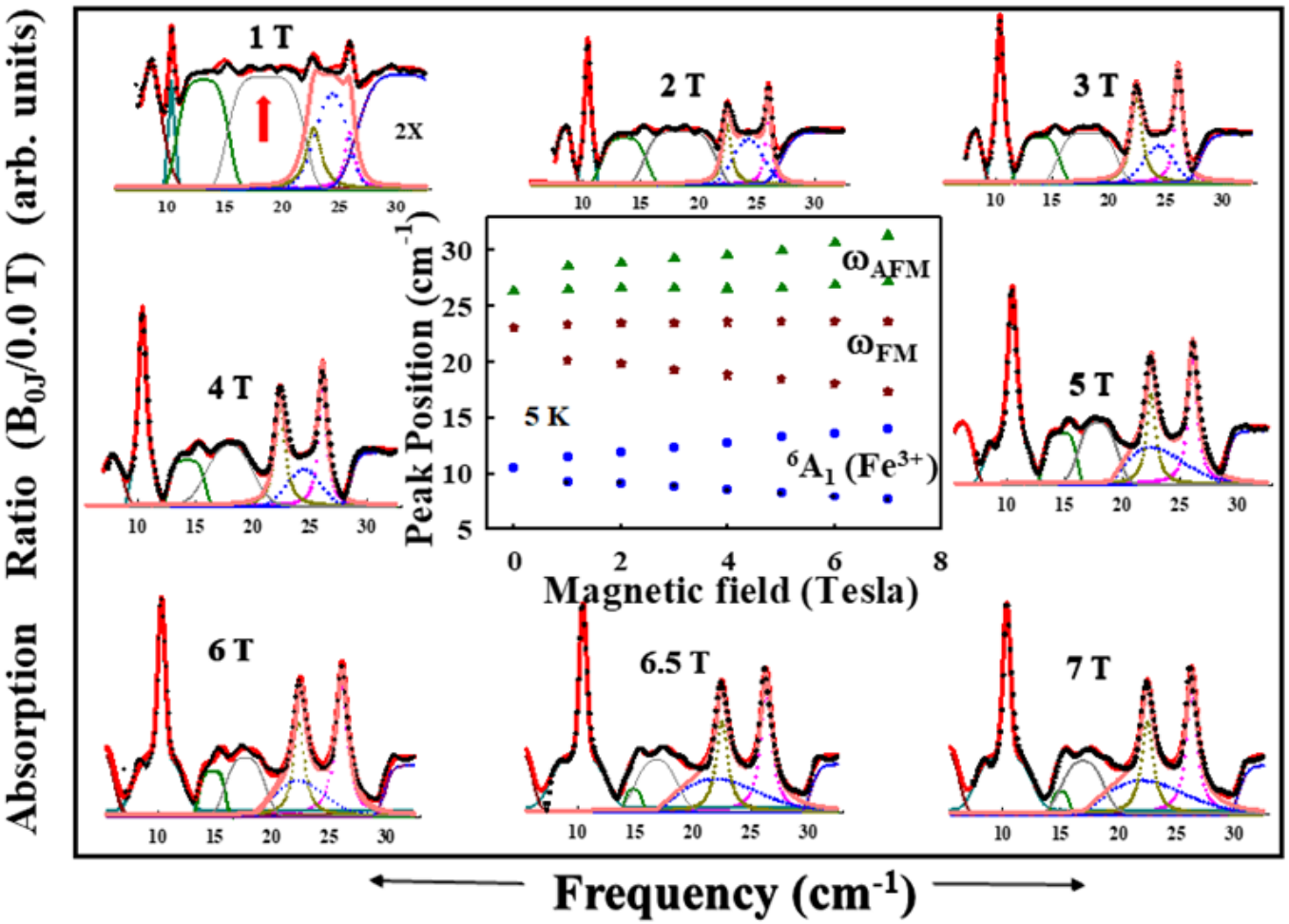

Fig. S10. Fe^{3+} ($^6A_1$) crystal field transition and ferromagnetic (ω_{FM}) and antiferromagnetic (ω_{AFM}) resonances of $LuFeO_3$ as function of the applied magnetic field. Insets: absolute field induced absorption ratios for $LuFeO_3$ from 1.0T to 7.0T at 5 K, dots: measurement; full lines: Gaussian and Weibull fits. The arrow at 1T signals secondary oscillations attributed to individual magnetic site contributions out of the two-site approximation. Center inset: peak positions of the shown absorptions.

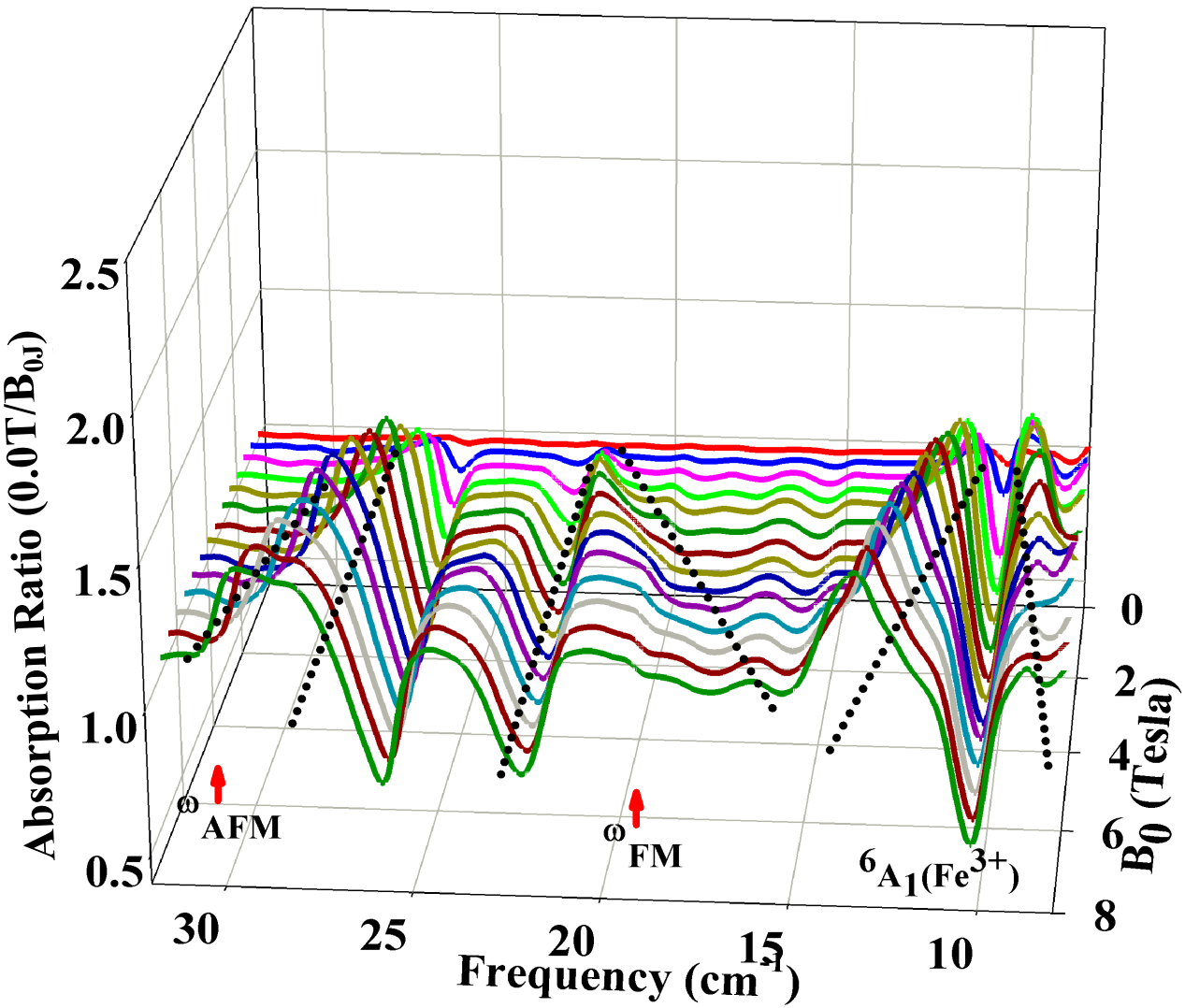

Fig. S11 Reciprocal view highlighting the field induced band split in the absorption ratios (B_{0J}/0.0T) of $LuFeO_3$ at 5 K.

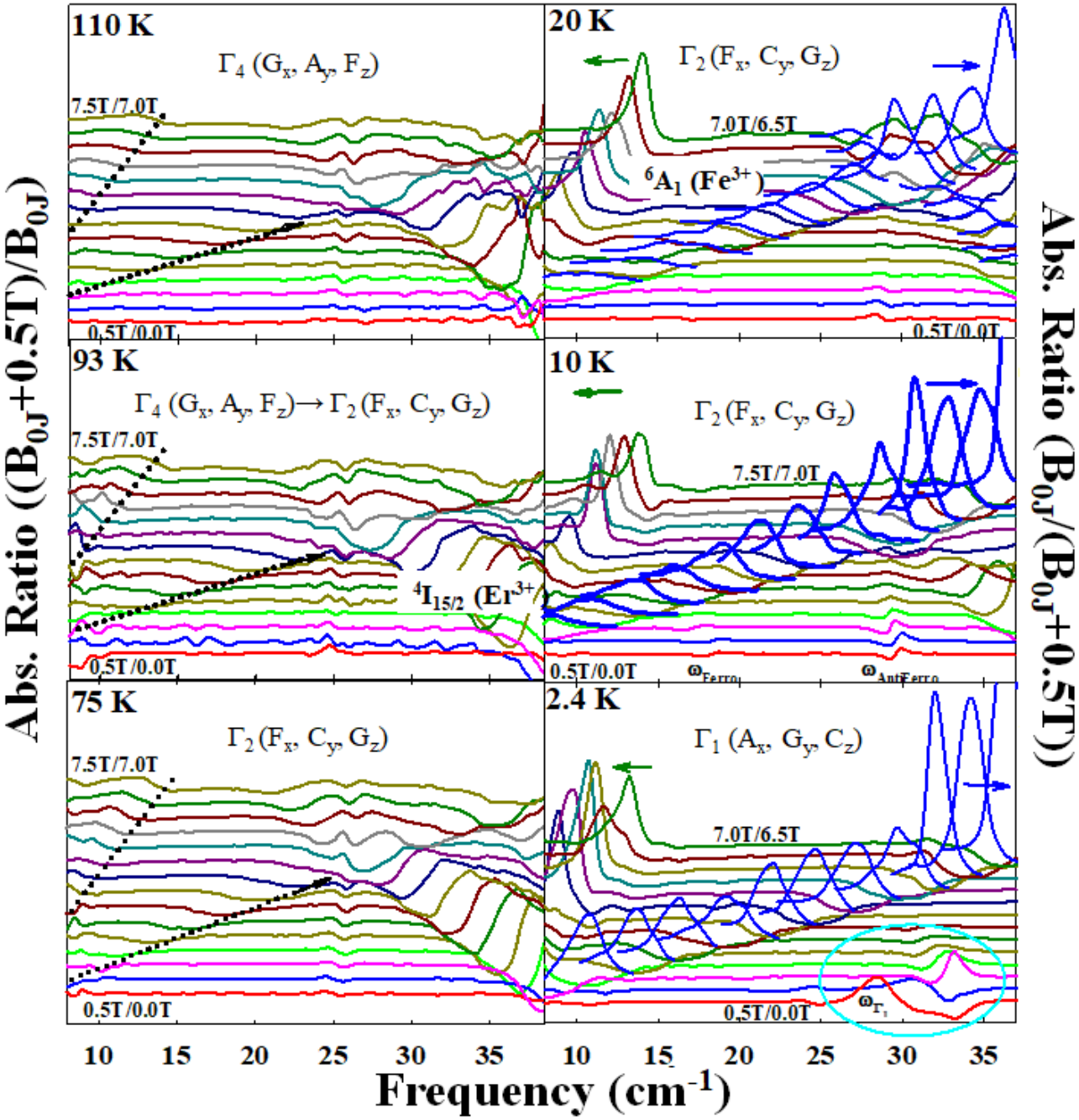

Fig. S12. Sequential absorption ratio spectra, $(B_{0j}+0.5T)/B_{0j}$, B_{0j} is the applied field at the jth incremental step, of $ErFeO_3$ crystal field Zeeman splits of Fe^{3+} ($^6A_1$) and Er^{3+} ($^4I_{15/2}$) multiplets and magnon modes from 110 K to 2.4 K in the Γ_4 (G_x, A_y, F_z), Γ_2 (F_x, C_y, G_z), Γ_1 (A_x, G_y, C_z) zero field magnetic phases. As it is discussed in the main text, the two resonances merge in the Γ_1 phase into one weaker broader single mode, shown encircled at 2.4 K, with a strong half-width at half-maximum field dependence.

a) Far infrared measurements

Far infrared near normal reflectivity spectra using conventional near normal incidence geometry were taken at the CEMHTI (Conditions Extrêmes et Matériaux: Haute Température et Irradiation- UPR3079 CNRS-Orléans) facilities on heating from 4 K to 300 K at 1 cm^{-1} resolution with a Bruker 113V interferometer and at GREMAN (Groupement de Recherche Matériaux Microélectronique Acoustique Nanotechnologies- UMR 7347, Université François Rabelais Tours. Samples were mounted on the cold finger of a He- closed cycle refrigerator and a home-made He cryostat adapted to the near normal reflectivity attachment vacuum chamber of the interferometer. A liquid He cooled bolometer and a deuterated triglycine sulfate pyroelectric bolometer (DTGS) were employed to completely cover the spectral range of interest. A plain gold mirror and an in-situ evaporated gold film were used for 100% reference reflectivity.

We analyzed the reflectivity spectra using the standard procedures for multioscillator dielectric simulation given by,

$$\varepsilon(\omega) = \varepsilon_1(\omega) - i\varepsilon_2(\omega) = \varepsilon_\infty \prod_j \frac{(\omega_{jLO}^2 - \omega^2 + i\gamma_{jLO}\omega)}{(\omega_{jTO}^2 - \omega^2 + i\gamma_{jTO}\omega)} \qquad (1)$$

where $\varepsilon_1(\omega)$ is the real and the $\varepsilon_2(\omega)$ imaginary part of the dielectric function (complex permittivity, $\varepsilon^*(\omega)$), ε_∞ is the high frequency dielectric constant taking into account electronic contributions; and where ω_{jTO} and ω_{jLO}, are the transverse and longitudinal optical mode frequencies and with γ_{jTO} and γ_{jLO} their respective damping.[4]

We then fitted at every temperature the experimental near normal reflectivity by computing each with

$$R(\omega) = \left| \frac{\sqrt{\varepsilon^*}(\omega) - 1}{\sqrt{\varepsilon^*}(\omega) + 1} \right|^2 \qquad (2)$$

This allowed to extract the experimental phonon frequencies that were then matched to feature bands of the corresponding absorption spectrum.[5] With few exceptions our measurements agree with the 25 allowed infrared active zone center phonons [6, 7, 8] predicted for a compound with 4 molecules per unit cell (Z=4) sustaining the Pbnm space group. The irreducible representation is given by

$$\Gamma_{IR} = 7B_{1u} + 9B_{2u} + 9B_{3u} \qquad (3)$$

A broad feature appearing in the reflectivity of $ErFeO_3$ and $LuFeO_3$ at our lowest measuring limit assigned to a boson peak has been Gaussian fitted according

$$G = A * e^{-\sqrt{(x-Xc)}}/w \qquad (4)$$

where A is the intensity, Xc is its peak position, and w its width.[9]

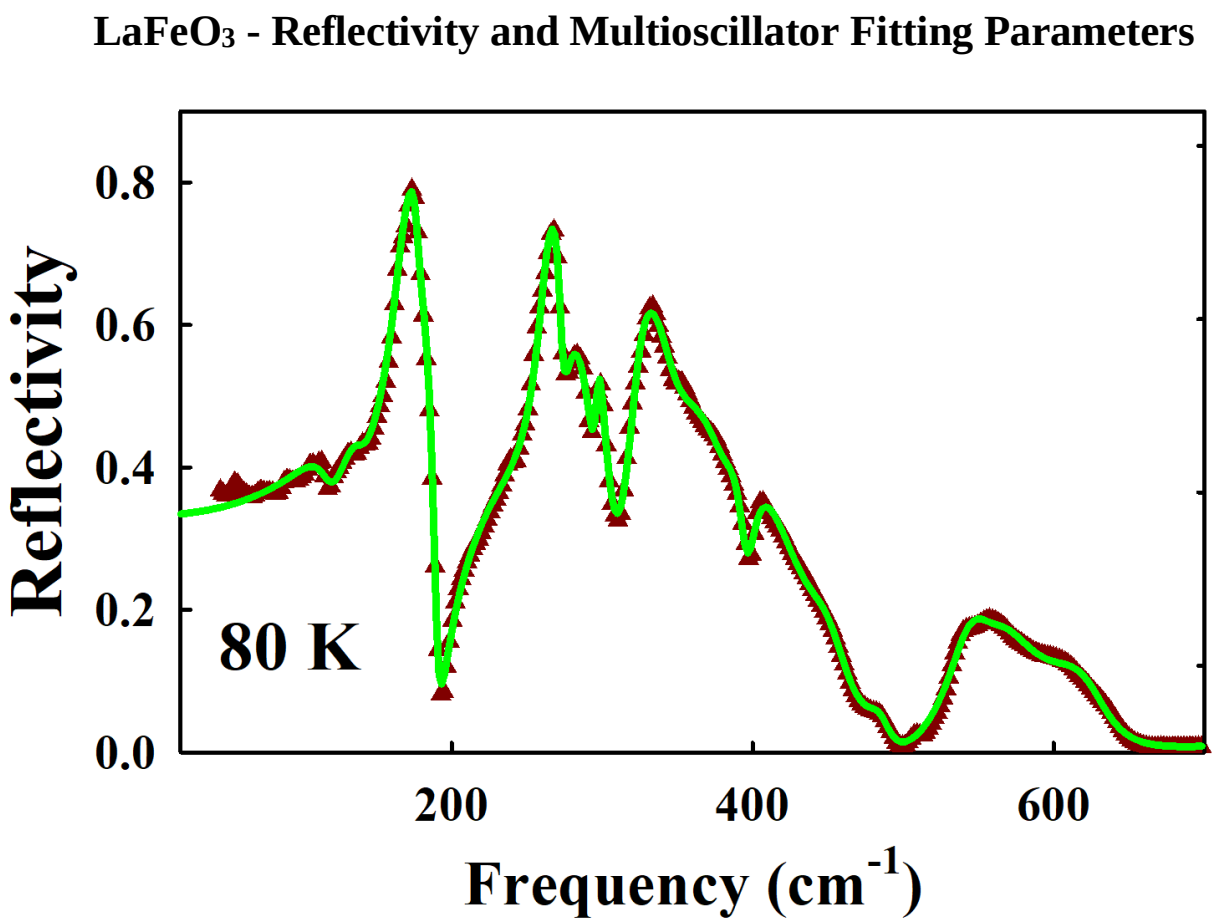

Fig. S13. $LaFeO_3$ near normal reflectivity at 80 K; experimental: upper triangles (showing 1 out of 10 points), full line: fit.

TABLE SI

Dielectric simulation fitting parameters for $LaFeO_3$ reflectivity at 80 K.

.

T (K)	ε_∞	ω_{TO} (cm^{-1})	Γ_{TO} (cm^{-1})	ω_{LO} (cm^{-1})	Γ_{LO} (cm^{-1})
80	2.65	117.0	27.4	119.7	21.0
		137.1	21.0	140.3	20.7
		164.8	13.1	117.8	6.3
		177.1	13.2	191.1	10.1
		231.8	74.9	254.8	61.5
		261.0	12.7	273.0	7.9
		275.1	13.6	285.9	8.4
		296.5	5.4	306.0	23.2
		321.2	17.2	344.9	36.3
		350.7	46.0	381.9	29.2
		384.5	27.4	395.1	12.3
		397.9	14.3	437.2	69.4
		445.8	40.7	467.5	40.5
		484.5	23.0	488.4	19.4
		540.0	29.6	558.2	35.7
		562.0	33.5	573.1	83.7
		615.8	57.3	630.8	42.8

$ErFeO_3$ Reflectivity and Dielectric Simulation Fitting Parameters

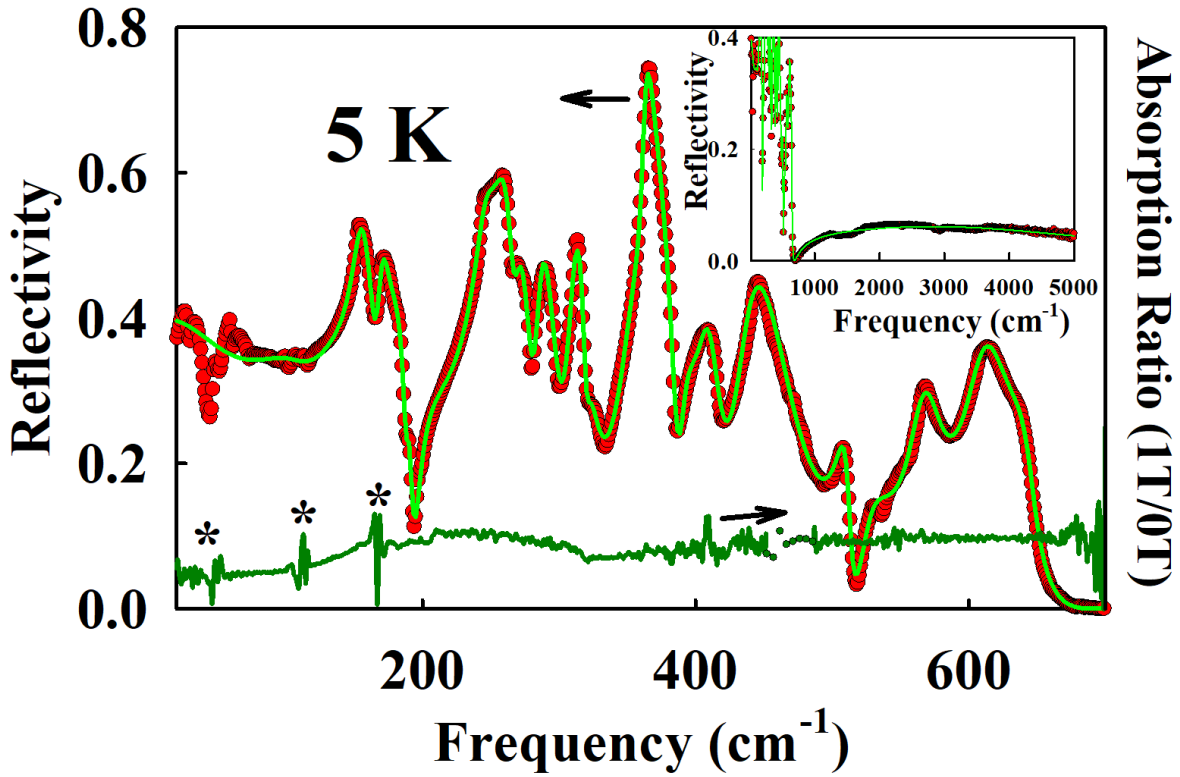

Fig. S14. Orthorhombic $ErFeO_3$ near normal reflectivity at 5 K, experimental: dots (showing 1 out of 10 points), full line: fit. Inset: full measured reflectivity range. The absorption ratio between 0 T and 1T spectra at 5 K is shown to emphasize the absence of a magnetic induced response at ~600 cm^{-1} breathing mode frequencies. Asterisks denote the Er^{3+} ($^4I_{15/2}$) crystal field energies.

Table SII

Dielectric simulation fitting parameters for $ErFeO_3$ reflectivity at 5 K. Bottom cells show the parameters used for the lower frequency Gaussian fit. Phonon frequencies appearing in the fits likely related to Er^{3+} ($^4I_{15/2}$) crystals field energies are indicated in bold italics with an asterisk.

(K)	ε_∞	ω_{TO} (cm^{-1})	Γ_{TO} (cm^{-1})	ω_{LO} (cm^{-1})	Γ_{LO} (cm^{-1})
5	1.24	****110.5***	***50.2***	***114.6***	***45.8***
		154.0	11.9	156.4	34.7
		156.0	73.7	166.0	10.7
		****169.2***	***7.6***	***175.7***	***19.6***
		179.2	19.8	187.8	4.5
		188.9	4.7	193.0	6.7
		197.6	26.5	207.4	76.1
		244.5	14.3	250.9	23.5
		257.0	19.0	265.9	9.8
		269.1	12.0	280.0	11.8
		285.5	9.7	299.9	20.0
		309.8	10.6	319.3	6.0
		320.3	8.4	326.3	27.9
		353.5	21.7	362.2	12.4
		361.8	6.2	386.1	10.7
		390.2	11.8	399.6	38.9
		406.4	18.4	415.4	23.6
		434.2	24.4	474.2	71.5
		509.2	18.8	513.2	7.6
		524.7	21.1	527,6	41.3
		562.3	24.6	573.1	34.4
		603.4	37.4	620.1	41.4
		642.3	80.3	644.7	14.4
		3731.9	4987.3	5438	8486.3
		A	Xc	w	
		470	11.1	30.5	

$ErFeO_3$ -Reflectivity and Multioscillator Fitting Parameters

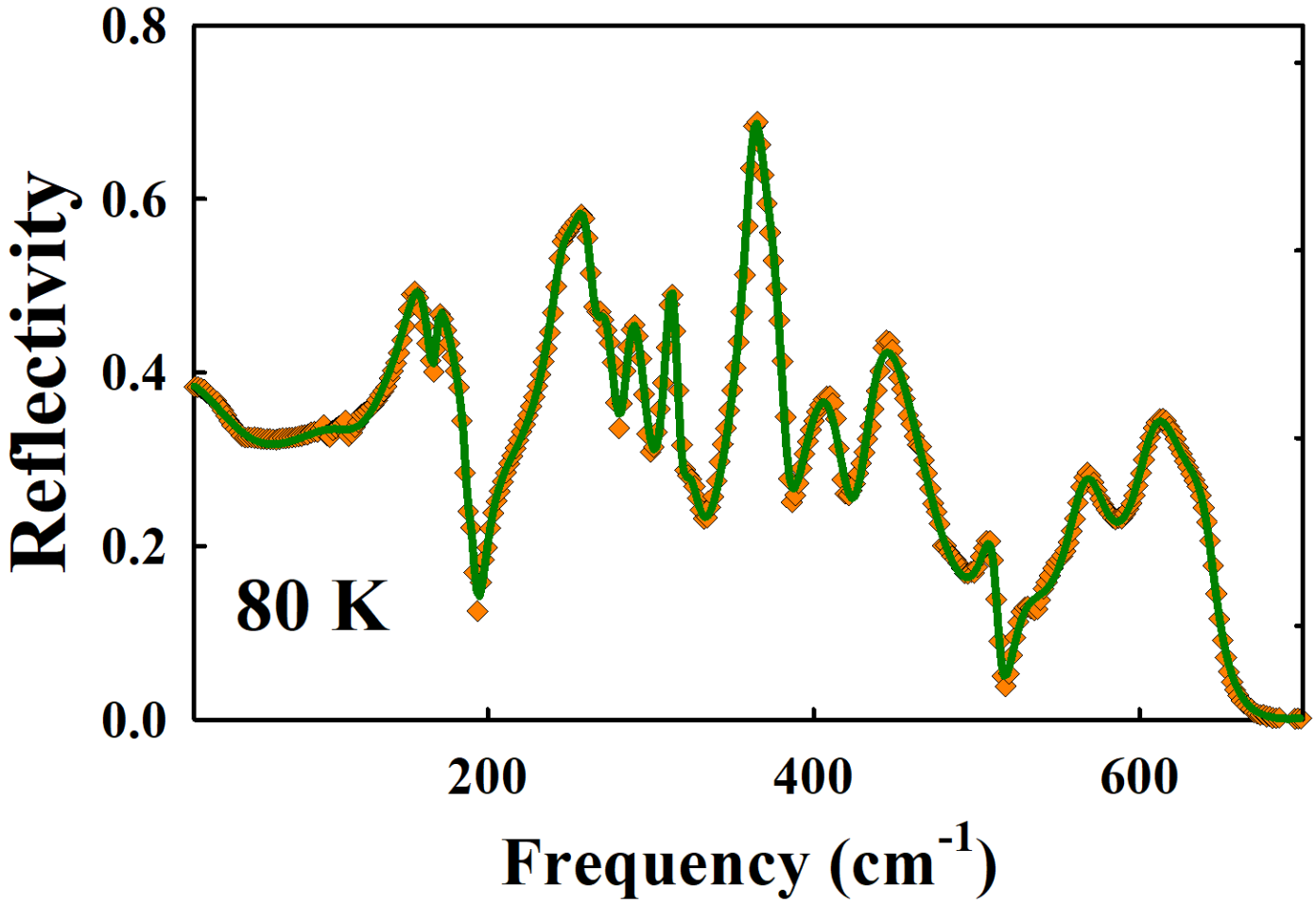

Fig. S15. $ErFeO_3$ near normal reflectivity at 80 K experimental: diamonds (showing 1 out of 10 points), full line: fit.

TABLE SIII

Dielectric simulation fitting parameters for $ErFeO_3$ reflectivity at 80 K. Bottom cells show the parameters used for the lower frequency Gaussian fit for an incipient boson peak shown in Fig. S15.

T (K)	ε_∞	ω_{TO} (cm^{-1})	Γ_{TO} (cm^{-1})	ω_{LO} (cm^{-1})	Γ_{LO} (cm^{-1})
80	1.22	116.0	49.3	120.1	42.5
		157.0	16.9	160.8	21.3
		162.5	35.4	166.9	7.3
		168.6	6.7	172.0	34.8
		173.4	47.5	187.6	2.7
		187.9	2.99	193.0	9.4
		197.5	27.7	206.8	85.7
		244.5	14.7	250.2	21.5
		256.0	17.0	265.0	12.3
		269.0	14.2	279.5	14.1
		286.2	11.4	299.3	22.0
		310.6	8.7	317.5	9.3
		322.1	13.6	327.3	20.4
		358.9	15.3	366.0	17.3
		360.4	11.5	382.4	13.2
		384.1	33.9	388.4	95.6
		399.8	45.4	420.6	24.1
		432.7	22.7	475.2	71.0
		509.2	19.5	513.2	8.1
		522.4	22.3	524.1	44.3
		561.8	27.2	573.2	36.1
		602.4	354	617.1	40.6
		640.3	85.7	642.7	13.9
		3103.6	4753.4	4457.9	9553.0
		A	Xc	w	
		435.4	7.4	26.1	

$LuFeO_3$ -Reflectivity and Multioscillator Fitting Parameters

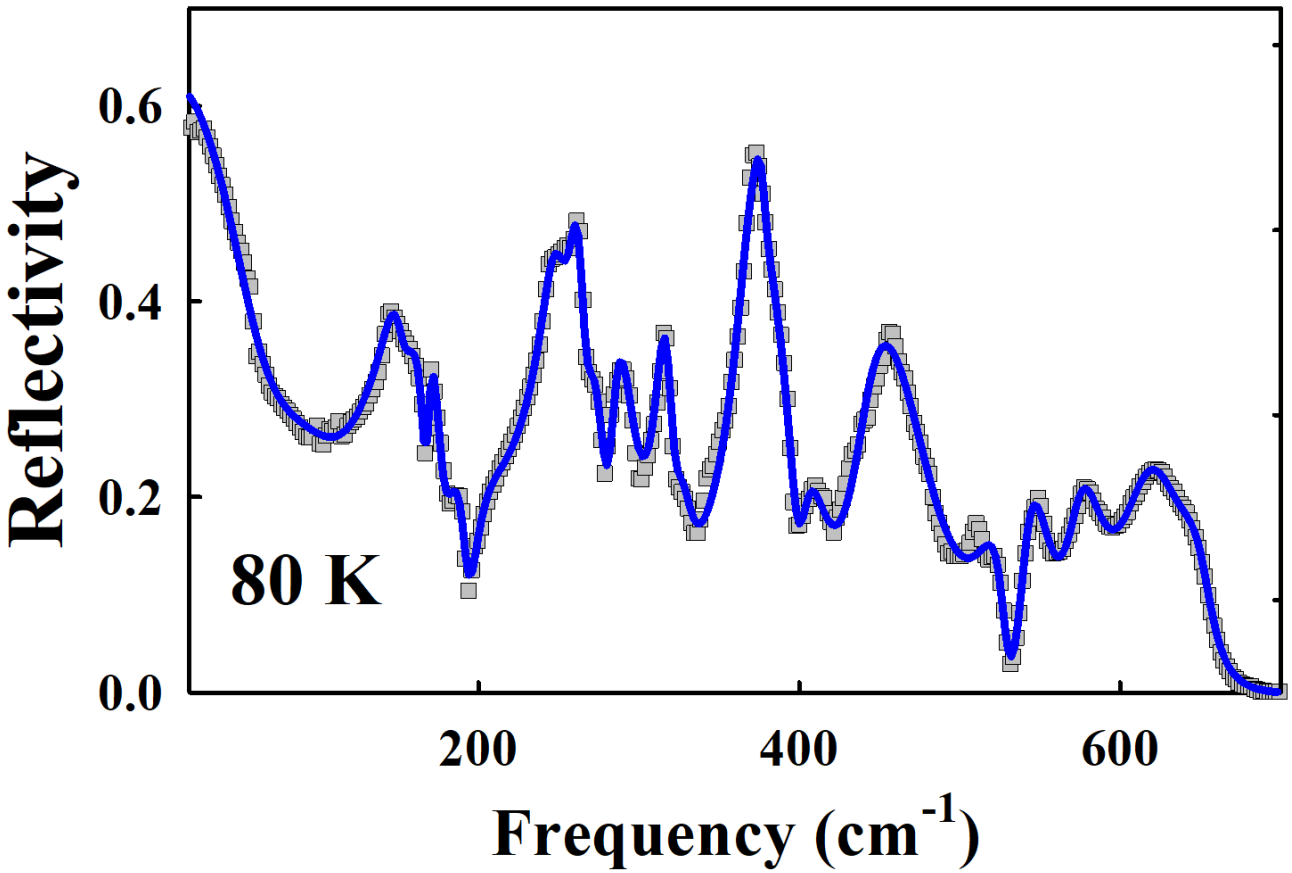

Fig. S16. $LuFeO_3$ near normal reflectivity at 80 K; experimental: squares (showing 1 out of 10 points), full line: fit. Note the increase in reflectivity toward lower frequencies indicates a boson peak known to be associated to structural inhomogeneity, unreleased strains, and potential freer charges localized in grain boundaries or domain walls. [10]

TABLE SIV

Dielectric simulation fitting parameters for $LuFeO_3$ reflectivity at 80 K. Bottom cells show the parameters used for the lower frequency Gaussian fit for the boson peak shown in Fig. S16.

T (K)	ε_∞	ω_{TO} (cm^{-1})	Γ_{TO} (cm^{-1})	ω_{LO} (cm^{-1})	Γ_{LO} (cm^{-1})
80	1.14	108.7	90.5	116.2	64.5
		148.5	23.6	155.1	5.7
		160.5	6.6	163.8	21.8
		169.4	6.1	177.3	13.3
		187.6	21.2	193.4	10.0
		245.9	15.7	253.7	18.2
		259.6	12.2	269.4	11.7
		269.8	16.8	280.2	133.8
		285.2	11.0	298.2	29.8
		314.2	11.7	321.0	10.9
		325.1	14.1	329.4	21.2
		365.8	18.7	377.7	8.9
		368.2	83.0	374.2	61.5
		377.2	10.4	398.4	13.8
		402.7	14.1	415.4	43.5
		440.7	29.3	486.3	68.7
		522.7	31.4	528.5	11.5
		540.2	13.6	553.7	33.7
		571.7	22.0	581.5	35.9
		608.8	42.1	630.5	41.8
		648.9	43.8	652.3	18.0
		3997.7	12126.6	5551.0	25947
		A	Xc	w	
		3228.1	10	24.0	

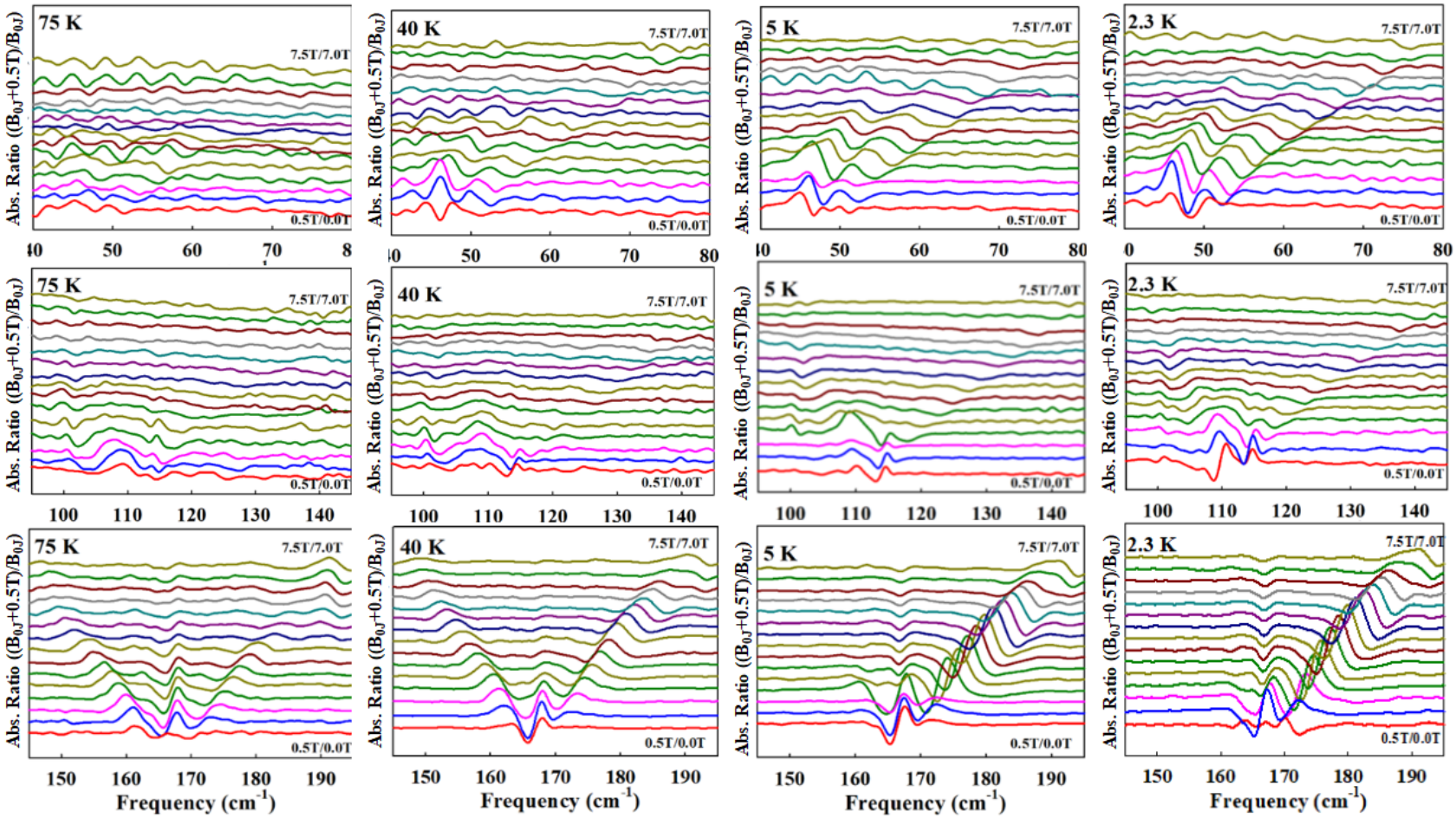

Fig. S17. Polyethylene pellet $ErFeO_3$ embedded sequential absorption ratio spectra, $(B_{0j}+0.5T)/B_{0j}$, B_{0j} is the applied field at the jth incremental step, of ground crystal field multiplet Er^{3+} ($^4I_{15/2}$) zero field cooled at 46 cm^{-1}, 114 cm^{-1} and 168 cm^{-1} in the Er^{3+} paramagnetic and antiferromagnetic phases showing the biased distortion due to the Fe^{3+} ($^6A_1$) magnetic exchange below the compensation temperature ~40 K. Spectral noise is understood in terms of the population temperature dependence according Boltzmann statistics for the respective levels.

REFERENCES

1. https://www.helmholtz- Berlin.de/pubbin/igama_output?modus=einzel&gid=1691&sprache=de

2. K. Holldack, and A. J. Schnegg, THz electron paramagnetic resonance / THz spectroscopy at BESSY II, Journal of Large-Scale Research Facilities **2**, A51. http://dx.doi.org/10.17815/jlrf-2-74.

3. M. Abo-Bakr, J. Feikes, K. Holldack, P. Kuske, W. B. Peatman, U. Schade, and G. Wu¨stefeld Brilliant, Coherent Far-Infrared (THz) Synchrotron Radiation Phys. Rev. Lett. **90** 094801 (2003).

4. T. Kurosawa, Polarization waves in solids, J. Phys. Soc. Jpn. **16**, 1298 (1961).

5. F. Gervais, Optical conductivity of oxides, Materials Science and Engineering **R39**, 29 (2002).

6. S. Smirnova, Normal modes of the $LaMnO_3$ Pnma phase: comparison with La_2CuO_4 Cmca phase, Physica B **262**, 247 (1999).

7. M. N. IR. L. Whiteliev, M. V. Abrashev, H.-G. Lee, V. N. Popov, Y. Y. Sun, C. Thomsen, R. L. Meng, and C. W. Chu, Raman spectroscopy of orthorhombic perovskite like $YMnO_3$ and $LaMnO_3$, Phys. Rev. B **57**, 2872 (1998).

8. A. Chopelas, Single-crystal Raman spectra of $YAlO_3$ and $GdAlO_3$: comparison to several orthorhombic ABO_3 perovskites, Phys. Chem. Minerals **38**, 709 (2011).

9. Focus software, http://cemhti.cnrs-orleans.fr/pot/software/focus.html

10. R. Milkus and A. Zaccone, Local inversion-symmetry breaking controls the boson peak in glasses and crystals, Phys. Rev. B **93**, 094204 (2016).